國立臺灣大學化學研究所

博士論文

Department of Chemistry

College of Science

National Taiwan University

Doctoral Dissertation

合成碲化鐵與石墨烯奈米材料及其於感測和光催化之應用

Synthesis of Iron Telluride and Graphene based Nanomaterials

for Sensing and Photocatalytic Applications

羅伊

Prathik Roy

指導教授：張煥宗 博士

共同指導教授：梁啟德 博士

Advisor: Huan-Tsung Chang, Ph.D.

Co-Advisor: Chi-Te Liang, Ph.D.

中華民國 102 年 6 月

June, 2013

國立臺灣大學博士學位論文
口試委員會審定書

（論文中文題目）合成碲化鐵與石墨烯奈米材料及其於感測和光催化之應用

（論文英文題目）Synthesis of Iron Telluride and Graphene based Nanomaterials for Sensing and Photocatalytic Applications

　　本論文係 羅伊君（學號 D98222029 ）在國立臺灣大學化學系完成之博士學位論文，於民國 102 年 6 月 27 日承下列考試委員審查通過及口試及格，特此證明。

口試委員：

＿＿＿＿＿＿＿＿＿＿＿＿＿＿（簽名）
（指導教授）

＿＿＿＿＿＿＿＿　　　＿＿＿＿＿＿＿＿

＿＿＿＿＿＿＿＿　　　＿＿＿＿＿＿＿＿

系主任、所長 張煥宗 ＿＿＿＿＿＿＿＿＿＿（簽章）
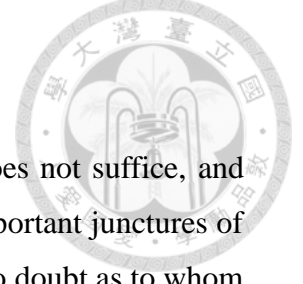
Acknowledgement

Ever so rarely, there comes occasions where a mere thank you does not suffice, and this is one such occasion. I stand at the cusp of one of the most important junctures of my life and there are so many people to thank. There is however, no doubt as to whom I would like to thank first. Prof. Chang and Prof. Liang, there are a lot of things I could say right now, but none of it would be apt for the immense gratitude I feel for you both. In India, we place our guru's (advisor) above all else. Toward the end, when the gurus think it is the right time for his student to step out into the world. The student sings the "guru-mantra" for them.

Tvam-Eva Maataa Ca Pitaa Tvam-Eva |
Tvam-Eva Bandhush-Ca Sakhaa Tvam-Eva |
Tvam-Eva Viidyaa Dravinnam Tvam-Eva |
Tvam-Eva Sarvam Mama Deva Deva ||

I know of no better way to thank you both than to sing the guru-mantra for both of you. The mantra in Sanskrit, the oldest known language in the world translates to:

You Truly are my Mother And You Truly are my Father .
You Truly are my Relative And You Truly are my Friend.
You Truly are my Knowledge and You Truly are my Wealth.
You Truly are my All, My God of Gods.

Albert Schweitzer, a noted German musician and philosopher once said:

"At times our own light goes out and is rekindled by a spark from another person. Each of us has cause to think with deep gratitude of those who have lighted the flame within us."

And there are so many people who have ignited this spark over the course of my life. It is very difficult for me to mention each and every one, for that I hope they forgive

me. I hope though, if they were to come across my thesis in a dusty old library at some point of their life. I am sure they would know who they are.

Prof. Murthy, (Director of Nanotechnology, N.I. University, India) has always been my pillar of support; in fact I wouldn't be here in Taiwan pursuing my Ph.D. if it were not for him teaching me, egging me and inspiring me to aim higher. To say thank you would never be enough, I hope I can repay the debt of gratitude I owe you someday. I would like to thank Prof. Chih Ching Huang (Professor, Institute of Bioscience and Biotechnology, National Taiwan Ocean University) for his guidance and support throughout my Ph.D. career. I am also grateful for the opportunity Prof. Ren Jang Wu (Chairman, Dpt. Of Chemistry, Providence University, Taiwan) provided me for carrying out research in his lab. I would also like to express my thanks to Dr. Joeseph Joly for his hospitality and sharing his research expertise during my trip to India for the Indo-Taiwan Project.

My first steps into Science were due to my school teachers, especially Malathi Ma'am, Gopalkrishnan Sir and Sharada Mam. There have been so many others who have nurtured me and taught me like their own child. I am grateful for their love and encouragement and thank them from the bottom of my heart. Loyola College was where I started the journey toward Science and Chemistry and right at the forefront were Dr. D. Suresh Kumar (Professor, Department of Chemistry, Loyola College, Chennai, India), Dr. Jeya Rajendran (Professor, Department of Chemistry, Loyola College, Chennai, India) and Dr. Judith Vijaya (Professor, Department of Chemistry, Loyola College, Chennai, India). They were my mentors in every sense of the word. The base on which I stand today is due to them and for that I owe them my deepest gratitude.

I am highly thankful to two gentlemen and research scholars Dr. Zong-Hong Lin (Post-Doctoral Fellow, Georgia Institute of Technology, U.S.A) and Dr. Arun Prakash Periasamy (Post-Doctoral Fellow, National Taiwan University, Taiwan) who have taught me, inspired me and treated me like their younger brother during the course of my doctoral career. I don't think I would be where I am without both of you.

A friend in need is a friend in deed is how the saying goes, and where would I be without friends. Chiashain, my friend I don't think it would be right of me to thank you as no amount of thanks would be enough to express how grateful I am for your friendship. And to all my other friends from all around the world, you know who you are. I love you all and I am thankful for all your friendship.

There is always that one person though at the end of the day, that you can count on to fall back upon during hard times, the difficult times and share the joys of the good times. And that one constant in my life has always been Rini. You know my respect, love and gratitude for you and it will always be the same.

I sincerely acknowledge the Taiwan government and National Taiwan University, Taiwan for providing me with the International Graduate Scholarship and the Graduate Support Fund. I am thankful to the College of Science for providing me the International Graduate Fellowship. I also extend my thanks to National science council of Taiwan and Department of Science and Technology, India for the Indo-Taiwan Project Funds. I am thankful to Rotary International for providing me the International Rotary Scholarship. It is my immense pleasure to thank all the faculty members in the department of Chemistry and Physics in NTU, also other staff members in office of international affairs, and department of Chemistry office in NTU for all their valuable help.

My two cousin sisters, Reshmi Banerjee and Pritha Roy, I love you both for standing by me during the tough times and constantly encouraging me throughout my research career.

I cannot possibly thank my parents enough for their prayers, their love, their encouragement, and for just being there for me day in and day out, Mr. Ajoy Roy and Mrs. Rita Roy, thank you for bringing me to this world. Thank you for all the joy that you have given me, thank you for your blessings. I would consider myself blessed if I could make you as happy as you have always made me. It is my turn to do so now.

Dedicated to Ajoy and Rita Roy, my beloved parents.

中文摘要

本論文主要是利用合成的奈米材料來偵測血液樣品中葡萄糖及汞離子濃度,且應用奈米材料之光觸媒活性進行高毒性污染物如硝基苯的降解。論文分成四個章節,第一章內容包括奈米材料作為感測器的背景簡介、以奈米材料類酵素活性的概念設計比色型生物感測器,及半導體型光觸媒應用於環境復育的介紹。第二章以電化學方法將碲奈米線合成具有類過氧化酶活性的碲化鐵奈米棒(FeTe nano rods)。當有過氧化氫的存在時,碲化鐵奈米棒對過氧化酶之受質—ABTS 具有極高的催化活性,此催化機制可應用於偵測過氧化氫及葡萄糖的濃度,對兩者的偵測極限和線性範圍分別是(55 nM;0.1-5 μM)和(0.38 μM;1-100 μM),其偵測效果優於其他由鐵所製備的奈米材料及辣根過氧化酶。而碲化鐵奈米棒的高催化活性推測可能是反應中鐵離子的釋出扮演重要角色。第三章是利用碲化鐵奈米棒與汞離子之間的陽離子交換反應,根據其顏色的變化,設計可偵測血液中汞離子的比色型生物感測器,其偵測極限為 1.31 nM,訊雜比為3,線性範圍 5-100 nM,顯示此系統對汞離子具有高度選擇性。在最後一章中,以簡便的水熱法合成石墨烯—氧化鋅—金的奈米複合體 (G-ZnO-Au NC),此材料在紫外光照射 140 分鐘的條件下,可將硝基苯還原成苯胺,且產率高達 98 %,相較於市售的二氧化鈦及氧化鋅奈米球,此複合體催化活性高於此兩種材料分別為 3.5 及 4.5 倍。此外,石墨烯—氧化鋅—金的奈米複合體在經過五次重覆反應後,其轉換效率只降低 7 %,顯示此材料具有極佳耐久性。研究石墨烯—氧化鋅—金的奈米複合體將硝基苯還原成苯胺的反應機制,數據顯示在無氧環境下,還原反應的效率可達到最高,其主要的原因可能是氧氣會競爭被光子激發的電子,進而影響材料的光催化活性。由於石墨烯—氧化鋅—金的奈米複合體光觸媒具有降解有毒污染物的特性,相信未來有極大的潛力應用於環境復育上。

關鍵字:鐵—碲奈米棒、類酵素活性、比色型生物感測器、毒理學、半導體型光

Abstract
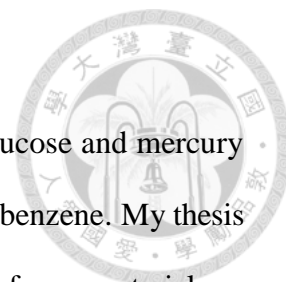
This thesis focuses on synthesizing nanomaterials for sensing of glucose and mercury in blood, and photocatalysis of highly toxic pollutants such as nitrobenzene. My thesis is divided into four parts. Chapter one introduces the background of nanomaterials as sensors, the concept of enzyme mimics for colorimetric bio-sensing purposes, as well as an introduction to semiconductor photocatalysts, unique properties offered by photocatalytic nanomaterials for environmental remediation. In chapter two, iron telluride nanorods (FeTe NRs) were prepared from Te nanowires through a galvanic reaction, that act as enzyme mimics and possesses strong catalytic activity towards the oxidation of a peroxidase substrate (ABTS) by H_2O_2, enabling the detection of H_2O_2 and glucose with a limit of detection (LOD) of 55 nM (linear range = 0.1-5 µM) and 0.38 µM (linear range = 1-100 µM) respectively, which is better than other iron based nanomaterials and horse radish peroxidase (HRP). It is also found that the release of Fe^{2+} ions plays a critical role in the high catalytic activity. The third chapter utilizes the FeTe NRs based system for the detection of mercury with a limit of detection of 1.31 nM at a signal-to noise ratio of 3 and a linear range of 5 to 100 nM ($R^2 = 0.99$), through a cation exchange reaction between FeTe NRs and Hg^{2+} as a colorimetric biosensor for total mercury in blood. The sensing system exhibits excellent sensitivity for mercury. The final chapter deals with the development of graphene-ZnO-Au nanocomposite (G-ZnO-Au NC) through a simple hydrothermal approach, which acts as a highly efficient photocatalyst under UV light for the reduction of nitrobenzene to aniline under 140 min with an yield of ca. 98 %. The photocatalytic activities of the nanocomposite are 3.5 and 4.5 fold higher than that of commercial TiO_2 and ZnO nanospheres (NSs) respectively, it also exhibits excellent durability with a decrease of only 7% in the conversion efficiency after 5 cycles. A detailed study on the mechanistic path of the

photocatalytic reduction reveals that reduction of nitrobenzene to aniline is most efficient in the absence of oxygen, as oxygen tends to compete for the photo-generated electrons. G-ZnO-Au NC photocatalyst has the potential to find real world applications in the near future for environmental remediation.

Keywords: iron telluride nanorods, enzyme mimics, colorimetric biosensors, toxicology, semiconductor photocatalysts, graphene-ZnO-Au nanocomposites nitrobenzene, environmental remediation.

Contents

Efficient Photocatalytic Reduction of Nitrobenzene

Figure Contents

XII

XIII

Five measurements were conducted for each sample.

Scheme Content

Table Content

XV

Chapter 1

Introduction

1.1 Nanotechnology

Innovation in technology started from the Stone Age, when human beings in their most primitive form invented the wheel. The fundamentals of technology have evolved from tasks which were once seen as implausible to common everyday chores and tools. The last century has seen some of the most important theoretical and experimental concepts in the field of science and technology with developments and progress in molecular technology spawning a new form of technology: Nanotechnology. K. Eric Drexler brought forth the idea of nanotechnology which he defines as "Technology based on the manipulation of individual atoms and molecules to build structures to complex atomic specifications". This technology defined by Drexler, is of the order of 'nano' (100 nanometers, or a billionth of a meter). Such fine structures are only visible with powerful microscopes such as scanning tunneling microscope (STM) or tunneling electron microscope (TEM) which enables scientists to not only peep into the deepest parts of the molecules, but also pick up, arrange atoms and place them at their will.[1]

Nanomaterials such as Iron-based chalcogenides (FeTe, Iron Telluride) have found use in not only superconductors, but also as enzyme mimics.[2] Graphene, a wonderful material, has been at the forefront of research and has given its inventors the Nobel Prize, due to its amazing electron transport, strength and the ability to make composites that can be used as highly efficient photocatalysts.[3] At the cutting-edge of research, nanotechnology has a significant impact on almost all industries and areas of society. It helps us build a better world with long lasting, cleaner, safer, and smarter materials in the field of medicine, engineering, agriculture and for industry in general. As a result of recent improvement in technologies to see and manipulate these materials, the field has seen a huge increase

in funding from private enterprises and government, and academic researchers within the field have formed many partnerships.[1]

1.2 Nanomaterials as Biosensors

1.2.1 The Concept of Enzyme Mimic

"One of the great intellectual challenges presented to Science by Nature is a proper understanding of how enzymes work. At one level we can 'explain' enzyme catalysis by the ability of an enzyme to bind and thus stabilize selectively the transition state for a particular reaction. But our current level of understanding fails the more severe, practical test that of designing and making artificial enzyme systems with catalytic efficiencies which rival those of natural enzymes." – An introduction given by A. J. Kirby was the highlight on which the ideas of artificial enzyme systems have taken fruition in order to attain catalytic efficiency rivaling that of natural enzymes.[4]

The question we ask ourselves is how do these enzymes work? While also trying to figure out and replicate studies of binding and catalysis in simpler, artificial systems. Enzymes however are not merely highly evolved catalysts; they are multifaceted and thus have more than one role to play such as both recognizing and responding to molecules other than their specific substrate and product, as part of the control mechanisms of the cell. Natural enzymes though bear some serious disadvantages, such as the inhibition of its catalytic activity. Moreover, the preparation, purification and storage of natural enzymes are usually time-consuming and expensive; this is where the synthesis of artificial enzyme mimics using nanomaterials have evolved with the objective of efficient combination of binding and catalysis.[5] To begin with, the ability to bind efficiently and determine the mechanism

involved is required, since it is the rate-determining transition state which is the most important target for the binding process.[6] Ultimately the two methodologies must congregate if a genuine enzyme mimic is to transpire. There is great promise in such nanomaterial based enzyme mimics which may be more robust than proteins, for unnatural reactions of interest. However, in order to develop a successful enzyme mimic it is indispensable to use the concepts of a real enzyme.

1.2.2 The Mechanism behind Enzyme Mimics for Colorimetric Biosensing

Bio-sensing technology has taken significant strides with the help of a multitude of novel materials designed and fabricated for bio-sensing applications. The key challenge for colorimetric bio-sensing is transforming the detection events into color changes. To this end, a number of smart materials have been developed, including gold nanoparticles, magnetic nanoparticles, cerium oxide nanoparticles, carbon nanotubes, graphene oxide, and conjugatedmers, such as polythiophene derivatives or polydiacetylene, can change color upon conformational transition or aggregation have proved to be a valuable platform in a wide range of bio-sensing.[7] Nanomaterials, more so functionalized nanomaterials, have received significant attention in the recent past due to their large surface-to-volume ratio. Magnetic nanomaterials (such as Fe_3O_4) have been extensively studied and used in magnetic resonance imaging, drug delivery, biological separation, and even in biological catalysis. Such nanomaterials are thought to be chemically and biologically inert; which can then be functionalized with metal catalysts, enzymes, or antibodies. Surprisingly, Yan and coworkers found that Fe_3O_4 magnetic nanoparticles (MNPs) possessed an intrinsic enzyme mimetic activity similar to that of natural peroxidases.[8] There are a wide range of practical applications for such peroxidase activity such as

the ability to catalyze the oxidation of organic substrates in order to reduce their toxicity or bring about a color change which is then in turn used as a detection tool. The cynosure of such a nanomaterial is the production of Fe^{2+}/Fe^{3+} ions in the solution (Fenton's reagent) which subsequently catalyzes the breakdown of H_2O_2. Natural enzymes such as horse radish peroxidase (HRP) have such heme-containing centers.[8] These released Fe^{2+} ions are then used to catalyze the oxidation of a peroxidase substrate such as 2,2-azino-bis(3-ethylbenzothiazoline-6-sulfonic acid) or better known as ABTS as seen in Fig. 1.1. The mechanism proceeds as shown in the reactions below.
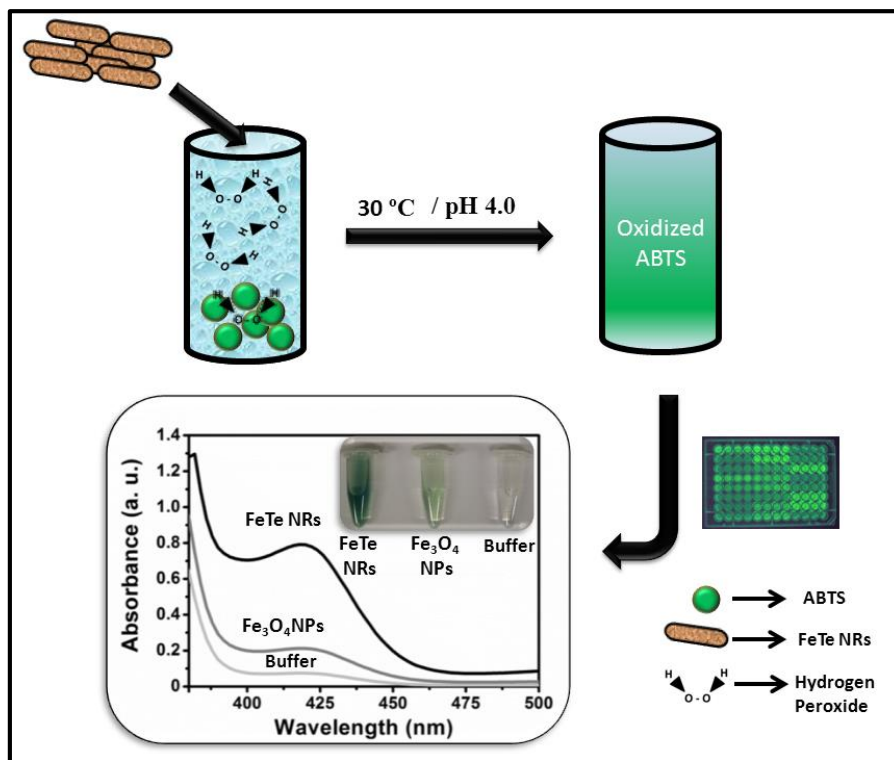
Fig. 1.1 Colorimetric sensing of glucose using FeTe NRs enzyme mimics.

$$H_2O_2 + ABTS \xrightarrow{Fe^{2+}} 2H_2O + oxidized\ ABTS \ - (1)$$

$$O_2 + Glucose \xrightarrow{GOx} H_2O_2 + gluconic\ acid \ - (2)$$
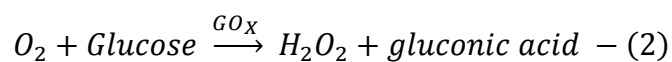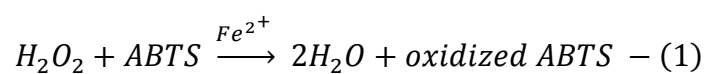
These easy and cost effective methods of detection show considerable benefits in comparison to conventional assays, predominantly in sensitivity, selectivity, and practicality. Since color changes can be read out by the naked eye, colorimetric bio-sensing does not require expensive or sophisticated instrumentation and can be applied to field analysis and point-of-care diagnosis.
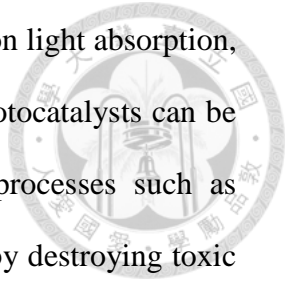
1.3 Semiconductor Photocatalysts

1.3.1 A Brief History on Semiconductor Photocatalysts

The word photocatalysis is a combination of two words, the prefix photo, defined as "light" and catalysis, the process of changing the rate of a chemical reaction without itself being involved in the reaction, thereby by reducing the activation energy needed for the reactant to form a product, the catalyst can increase the rate of the reaction. Semiconductor based photocatalysis under visible and ultraviolet light irradiation has been comprehensively studied for the quarter of the last century. Fujishimna and Honda in the year 1972 discovered the photocatalytic splitting of water on TiO_2 electrodes. This brought about the dawn of a new era in heterogeneous photocatalysis. Photocatalytic studies have largely investigated on the purification of water by the degradation of numerous organic pollutants and toxic substances. Quantum size effects on photoreactions for semiconductor nanoparticles have only been recently studied.[9]

Semiconductor photocatalysts mainly comprise of metal oxides such as TiO_2, ZnO, MnO_2 but are not limited to such materials, Au and other noble metals have met with considerable attention as well,[9] recently the use of graphene in semiconductor photcatalysts has been on the rise, with graphene providing exciting electron transport properties, which negates the drawbacks of traditional photocatalysts,[10] these

semiconductor photocatalysts can accelerate chemical reactions upon light absorption, typically sunlight. By utilizing the energy of absorbed photons, photocatalysts can be optimized to carry out a wide variety of important chemical processes such as environmental remediation – the process of purifying air or water by destroying toxic and other organic pollutants. Semiconductor photocatalysts have also found use in solar fuel cells, H_2 from water or methane/methanol from CO_2.[12] Various hybrid assemblies have been thought of to improve the performance of semiconductor photocatalysts by using semiconductor-semiconductor, semiconductor-metal, and semiconductor-reduced graphene oxide (RGO) nano-assemblies.[10] However, it is imperative for us to understand the intricate interface electron dynamics in all of these assemblies which will allow us to use these systems in various applications.

1.3.2 Photocatalytic Mechanism

The narrow band gap between the valence and conduction bands of a semiconductor have made it an ideal material for it to be used as photocatalysts. In order for photocatalysis to proceed, the semiconductors need to absorb energy equal to or more than its energy gap. This movement of electrons forms e^-/h^+ or negatively charged electron/positively charged hole pairs.[9] The hole can oxidize donor molecules. The excitation of electrons is accomplished by the absorption of photons of energy equal to or higher than the band-gap of their host material. This light-induced generation of electron-hole pairs is a prerequisite step in all semiconductor mediated photocatalytic processes. For example, when a photocatalyst such as titanium dioxide
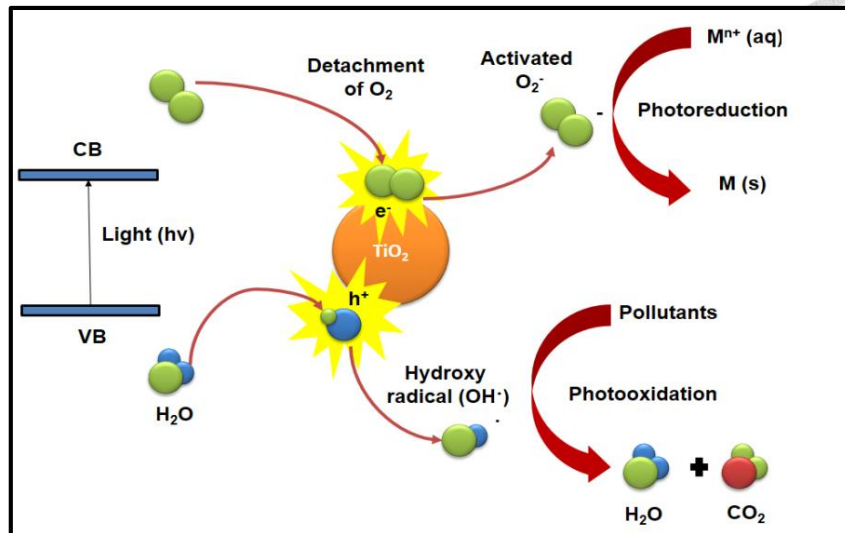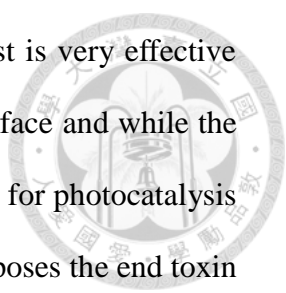
Fig. 1.2 Schematic representation of the photocatalytic mechanism

(TiO_2) absorbs ultraviolet (UV) radiation from sunlight or illuminated light source (fluorescent lamps), it will produce pairs of electrons and holes. The electron of the valence band of titanium dioxide becomes excited when illuminated by light. The excess energy of this excited electron promotes the electron to the conduction band of titanium dioxide therefore creating the negative-electron (e^-) and positive-hole (h^+) pair as illustrated in Fig. 1.2. This stage is referred to as the semiconductor's 'photo-excitation' state. The energy difference between the valence band and the conduction band is known as the 'Band Gap'. Wavelength of the light necessary for photo-excitation is: 1240 (Planck's constant, h) / 3.2 eV (band gap energy) = 388 nm. The positive-hole of titanium dioxide breaks apart the water molecule to form hydrogen gas and hydroxyl radical. The negative-electron reacts with oxygen molecule to form super oxide anion. This cycle continues when light is available.[9]

1.3.3 The Role of Semiconductor Photocatalysts in Environmental Remediation
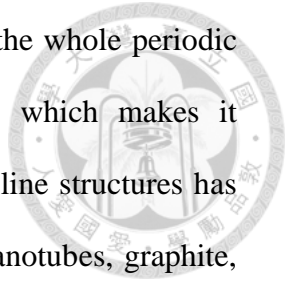
The use of a photocatalyst is not only restricted to killing bacterial cells, but

8

also decomposing the cell itself. The titanium dioxide photocatalyst is very effective as an antibacterial agent, even when there are cells covering the surface and while the bacteria are actively propagating, where Se/Te-TiO_2 NRs were used for photocatalysis induced actibacterial activity. The photocatalytic action also decomposes the end toxin produced at the death of cell. Titanium dioxide does not deteriorate and it shows a long-term anti-bacterial effect. Photocatalysts also act as highly efficient deodorizers. The hydroxyl radicals produced during the photocatalytic reaction accelerate the breakdown of many Volatile Organic Compounds (VOCs) such as formaldehyde, nitrogen dioxide, urine, fecal odor, gasoline, and many other hydro carbon molecules in the atmosphere by destroying the molecular bonds. This helps combine the organic gases to form a single molecule that is not harmful to humans thus enhancing the air cleaning efficiency.[9]

The photocatalytic reactivity of titanium oxides finds key use for the reduction or elimination of polluted compounds in air such as NOx, and cigarette smoke. It also exhibits high photocatalytic activity in the treatment of atmospheric constituents such as chlorofluorocarbons (CFCs) and CFC substitutes, greenhouse gases, and nitrogenous and sulfurous compounds. Photocatalyst coupled with UV lights can oxidize organic pollutants into nontoxic materials, such as CO_2 and water and can disinfect certain bacteria. This technology is very effective at removing further hazardous total organic compounds (TOCs) and at killing a variety of bacteria and some viruses in the secondary wastewater treatment. Pilot projects demonstrated that photocatalytic detoxification systems could effectively kill fecal coli form bacteria in secondary wastewater treatment.[9]

1.4 Graphene: How Playing With Sticky Tape Changed The World

Carbon is among the most flexible and robust elements in the whole periodic table. The fundamentals of organic chemistry are built on it, which makes it omnipresent in all living organisms on Earth. A plethora of crystalline structures has been developed around carbon: fullerenes or buckyballs, carbon nanotubes, graphite, diamond and, more recently, graphene. These materials are characterized by their dimensionality and the nature of the chemical bonding (sp^2 or sp^3) that keeps the atoms together. The main motif behind these structures is the hexagonal benzene ring.[10]

Graphene consists of a single layer of carbon atoms arranged in a two-dimensional (2D) honeycomb lattice. A range of well-known carbon materials such as three-dimensional (3D) graphite, one-dimensional (1D) carbon nanotubes, and zero-dimensional (0D) fullerene are built on the pillars of graphene. The unique properties of graphene such as its 2.3% absorption in the white light spectrum, high surface area, high Young's modulus, and excellent thermal conductivity has piqued interest from both academia and industry leading to applications in a wide range of areas, including high-speed electronic and optical devices, energy generation and storage, hybrid materials, chemical sensors, and even DNA sequencing as seen in Fig. 1.3.[11] The discovery of graphene by Konstantin Novoselov and Andre Geim were awarded the 2010 Nobel Physics Prize, giving rise to a research boom that is continuing.[11]
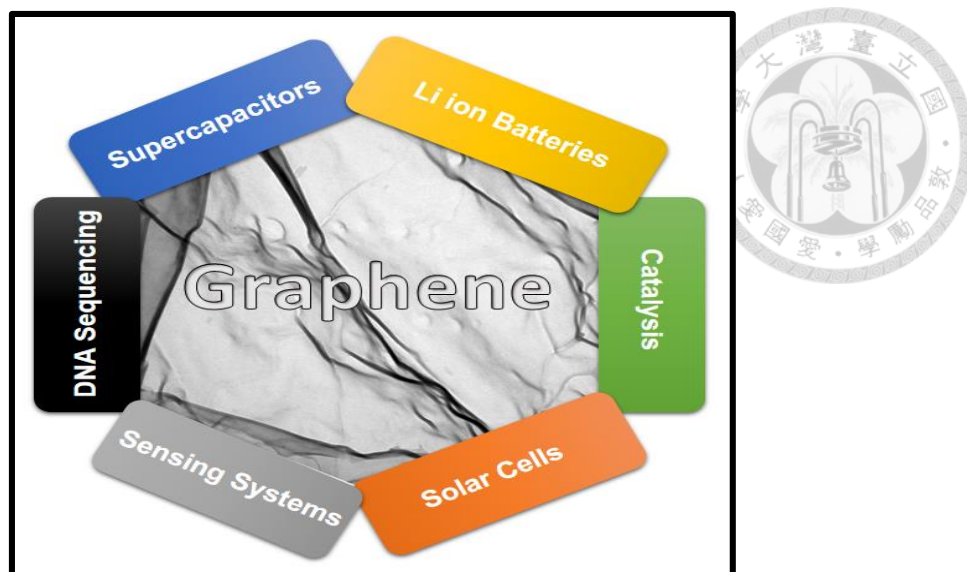
Fig. 1.3 Illustration of the various applications of graphene.

1.4.1 Graphene Based Semiconductor Photocatalysts

A great deal of attention has been paid towards the utilization of carbon based materials to enhance the photocatalytic activities of semiconductor photocatalysis in the recent past. There are a variety of advantages to incorporating carbon nanostructures in photocatalysts, for example they inhibit e^-/h^+ recombination (Fig. 1.4), provide greater support for the semiconductor photocatalyst and thus increasing the density of the photocatalyst itself. They also facilitates greater interaction and thus more active sites for adsorbing the analyte targeted for reduction or oxidation in its surface due to π-π conjugation.[14] Recent studies show the ability of graphitic carbon to form strong interfaces with TiO_2 through the formation of Ti–O–C bonds thereby extending the range in which it can absorb light.[15]

Various methods have been devised to incorporate metallic nanoparticles (e.g. Pt, Pd, and Au) loaded onto the surface of a carbonaceous material such as graphene or CNT. Which helps in stopping the recombination of holes and electrons and promoting an interfacial charge-transfer. On the other hand, doping with metal (e.g.

Fe^{3+}, Ru^{4+}, Mo^{6+}, Cr^{3+}, Sb^{5+} and V^{4+}) or nonmetal (e.g. N, F and S) helps in extending the photoresponse towards lower energy excitation through impurity levels between the conduction and valence bands of the main photocatalyst. Narrow band gap semiconductors such as CdS, CdSe, PbS, and Bi_2S_3 though can harvest visible light. However, large bandgap photocatalysts (TiO_2, ZnO, MnO_2) have gained more attention as they have found to be more efficient photocatalysts.[16]
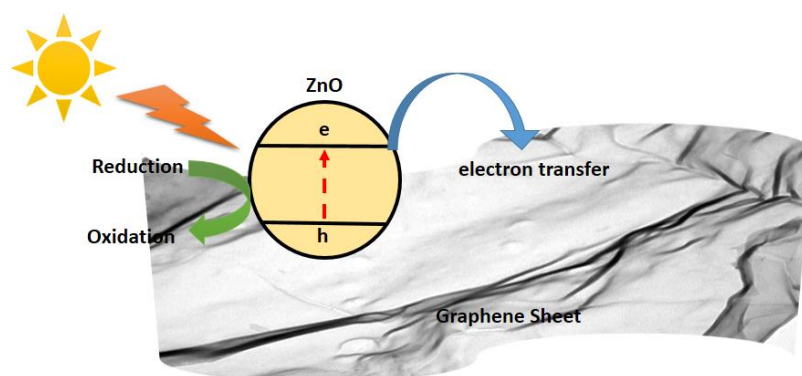
Fig. 1.4 Plausible electron transfer mechanism in graphene based semiconductor photocatalyst.
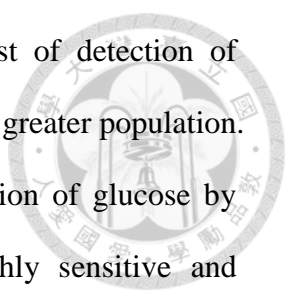
The incorporation of these photocatalysts on carbon-based materials involves critical understanding of various synthetic routes in order to achieve uniform morphology. Various strategies such as sol-gel, hydrothermal, microwave have been implemented to fine tune the properties of the product, including their electronic conductivity and storage capacity, hydrophilicity/hydrophobicity of the composites, morphology and porosity. All these parameters are of importance for many applications. However, a great number of these carbon based nanocomposites have been used for photocatalytic organic degradation, water splitting for hydrogen production, photovoltaic and photoelectrochemical cells, and antibacterial applications.[17-19]

1.4.2 Application of Graphene-Based Photocatalysts

Akhavan and co-workers have studied the antimicrobial activities of various graphitic carbons incorporating TiO_2 and ZnO. They found that the graphene based semiconductor photocatalyst showed enhanced photocatalytic activity toward the killing of Escherichia coli (*E. coli*) bacteria by a factor of 7.5 in an aqueous solution under sunlight.[20] Zhu and co-workers were able to extended the TiO_2's response into the visible range by coating thin layers of graphite-like carbon (~1 nm) on TiO_2 nanoparticles[21] due to electron coupling, resulting from the d–p interaction (d-orbital from the conduction band of TiO_2 and p states of graphite-like carbon). Yun's group further showed that graphitic carbon can shuttle electrons between two photocatalysts with complementary band structures to complete an electron cycle for Z-scheme water splitting.[22] A considerable amount of effort has also been put into photodegradation of organic pollutants and decoloration of organic dyes.[19, 22-23]

1.5. Motives of Research

At the crossroads of my scientific career I found myself wondering about the importance of pursuing research, more specifically research in chemistry. Think about it, without chemicals there is no universe, let alone life. We can all agree about the facts, but how can one convey the all-encompassing nature of chemistry in an exciting and informative way. My quest was to begin with isolating the fields I felt most strongly about, ideas that can actually be employed towards real world applications, this led to the detection of glucose in blood, as diabetes is a life-long disease marked by elevated levels of sugar (glucose) in the blood. It can be caused by too little insulin (a chemical produced by the pancreas to regulate blood sugar), resistance to insulin, or both. Approximately 347 million in the world have diabetes, 3.4 million of them as

a consequence of high glucose levels; however the average cost of detection of glucose is as high as USD 20 per test, which is unaffordable for the greater population. Hence it is imperative to find cheaper alternatives for the detection of glucose by synthesizing nanomaterials (FeTe NRs) that would enable highly sensitive and selective detection of glucose in blood. Environmental remediation through the detection of toxic elements has been another issue that has plagued mankind, as mercury is a notoriously toxic element that can damage DNA and disrupt the central nervous and endocrine systems. It is released into the environment through volcanic activity, coal production and industrial waste. Fish living in polluted water are particularly susceptible to poisoning, as the mercury can be taken in through the mouth or skin and becomes deposited in their organs. We went about preparing a simple colorimetric sensor based on the as-synthesized FeTe NR's with excellent sensitivity and selectivity for mercury in blood. However, mercury is not the only source of toxicity in the environment, chemicals such as nitrobenzene, which is the mainstay of chemical industries, is a massive problem for scientists to deal with in the pursuit of environmental remediation. Nitrobenzene is carcinogenic and genotoxic to human beings, causing diseases such as methaemoglobinaemia. It is therefore crucial that we found ways to curb this menace by degrading such chemicals. The best way to do so was to develop graphene based semiconductor photocatalysts such as G-ZnO-Au NC that allowed us to reduce the toxic nitrobenzene into aniline with close to 100 % yield and in quick time. In recent years it seems that the importance of science has declined. However its necessity in growing the economy and finding new solutions to old problems and dilemmas remain the same. Scientists find themselves at the crux of the problem or solution whichever way one wants to look at it, the choice of being able to solve a problem or create one lies squarely on our shoulders.

14

References

(1) Klabunde, K. J. *Nanoscale Materials in Chemistry*; Wiley-VCH: New York, **2001**.

(2) Roy, P.; Lin, Z.-H.; Liang, C.-T.; Chang, H.-T. *Chem. Commun.* **2012**, *48*, 4079-4081.

(3) Geim, A. K.; Novoselov, K. S. *Nat. Mat.* **2007**, *6*, 183-191.

(4) Kirby, A. J. *Angew. Chem. Int. Ed.* **1994**, *33*, 551-553.

(5) Kirby, A. J. *Angew. Chem. Int. Ed.* **1996**, *35*, 706-724.

(6) Jv, Y.; Li, B.; Cao, R. *Chem. Commun.* **2010**, *46*, 8017-8019.

(7) Randolph, L. M.; Chien, M.-P.; Gianneschi, N. C. *Chem. Sci.* **2012**, *3*, 1363-1380.

(8) Gao, L.; Zhuang, J.; Nie, L.; Zhang, J.; Zhang, Y.; Gu, N.; Wang, T.; Feng, J.; Yang, D.; Perrett, S. *Nat. Nanotech.* **2007**, *2*, 577-583.

(9) Linsebigler, A. L.; Lu, G.; Yates Jr, J. T. *Chem. Rev.* **1995**, *95*, 735-758.

(10) Geim, A. K.; Novoselov, K. S. *Nat. Mat.* **2007,** *6*, 183-191.

(11) Pumera, M. *Energy & Environ. Sci.* **2011,** *4*, 668-674.

(12) Baker, S.; Baker, G. *Angew. Chem. Int. Ed.* **2010,** *49*, 6726-6744.

(13) Shen, J.; Zhu, Y.; Yang, X.; Li. *Chem. Commun.* **2012,** *48*, 3686-3699.

(14) Robel, I.; Bunker, B. A.; Kamat, P. V. *Adv. Mater.* **2005**, *17*, 2458-2463.

(15) Li, Y.; Hwang, D.-S.; Lee, N. H.; Kim, S.-J. *Chem. Phys. Lett.* **2005**, *404*, 25-29.

(16) Linsebigler, A. L.; Lu, G.; Yates Jr, J. T. *Chem. Rev.* **1995**, *95*, 735-738.

(17) Iwase, A.; Ng, Y. H.; Ishiguro, Y.; Kudo, A.; Amal, R. *J. Am. Chem. Soc.* **2011**, *133*, 11054-11057.

(18) Mukherji, A.; Seger, B.; Lu, G. Q.; Wang, L. *ACS Nano* **2011**, *5*, 3483-3492.

(19) Ng, Y. H.; Lightcap, I. V.; Goodwin, K.; Matsumura, M.; Kamat, P. V. *J. Phys. Chem. Lett* **2010**, *1*, 2222-2227.

(20) Akhavan, O.; Ghaderi, E. *, J. Phys. Chem. C* **2009**, *113*, 20214-20220

(21) Zhang, L. W.; Fu, H. B.; Zhu, Y. F. *Adv. Funct. Mater.* **2008**, *18*, 2180-2189.

(22) Torimoto, T.; Okawa, Y.; Takeda, N.; Yoneyama, H. *Photochem. Photobiol., A,* **1997**, *103*, 153-157.

(23) Takeda, N.; Iwata, N.; Torimoto, T.; Yoneyama, H. *J. Catal* **1998**, *177*, 240-246.

Chapter 2

Synthesis of Enzyme Mimics of Iron Telluride Nanorods for the Detection of Glucose

2.1 Introduction

Hydrogen peroxide (H_2O_2) is involved in many chemical, biological, pharmaceutical, clinical, and environmental processes.[1] Detection of H_2O_2 and glucose by optical (absorption, chemiluminescence, and fluorescence), electrochemical (amperometry) and bioelectrochemical based sensing approaches are the most popular analytical techniques.[2-6] Although these methods have practical advantages, they suffer from serious drawbacks such as lack of sensitivity, rapidity, and/or specificity, problems such as time-consuming fabrication procedures, the need for expensive reagents, and/or the presence of serious matrix effects. Thus, rapid, accurate, reliable, sensitive, and cost-effective approaches for the detection of H_2O_2 are still needed.

Nanomaterials (NMs) such as Fe_3O_4,[7, 8] carbon,[9] and Au nanoparticles (NPs)[10] exhibit catalytic activity similar to that found in natural peroxidases, and have been successfully employed as enzyme mimics for the detection of H_2O_2,[7, 8] glucose,[7, 8] and xanthine,[10] respectively. NMs have distinct advantages in comparison to natural enzymes; including low cost, ease in preparation, stability, and superior surface to volume ratio.[11, 12]

The catalytic activity of these NMs comes from the released metal ions (e.g. Fe^{2+} and Au^{3+} ions) that catalyze the oxidation of the peroxidase substrates such as 2,2'-azino-bis(3-ethylbenzo-thiazoline-6-sulfonic acid) diammonium salt (ABTS). Unlike natural enzymes,[13] NMs usually lack specificity for analytes of interest. Thus, it is essential to prepare low-cost, environmentally friendly, specific, and active NMs as enzyme mimics.

In this work, we used Te nanowires (NWs) to prepare FeTe nanorods (NRs) through a spontaneous redox reaction between Te atoms and Fe^{3+} ions.[14-17] Te NWs

were synthesized from the reduction of tellurium dioxide (TeO$_2$) with concentrated hydrazine (N$_2$H$_4$).[14] FeTe has shown distinct properties of semiconductivity, superconductivity, and magnetism.[18, 19] While the physical properties of FeTe have come under intense scrutiny, biological applications of FeTe has not been studied yet. We investigated the enzyme mimetic property of the as-prepared FeTe NRs that catalyze the oxidation of ABTS with H$_2$O$_2$. Glucose oxidase (GOx), FeTe NRs, and ABTS were used to develop a greatly sensitive, robust and selective colorimetric detection system for the determination of glucose. Practicality was validated by the determination of glucose in blood samples.

2.2 Experimental Section

2.2.1 Chemicals

Sodium dodecyl sulfate (SDS, 99%), hexadecyltrimethylammonium bromide (CTAB, 99%), iron (III) chloride hexahydrate (99%); acetic acid (99.8%), L(+)-ascorbic acid (99%), dopamine (99%) and iodine (99.5%) were purchased from Acros (Geel, Belgium). Tellurium dioxide powder (99.9%), hydrazine monohydrate (80%), and hydrogen peroxide (35%) were purchased from SHOWA (Tokyo, Japan). Iron oxide (Fe$_3$O$_4$) nanoparticles (98%), fluorescein isothiocyanate (FITC, 90%), GOx, ABTS (99.8%), β-D-glucose (99%), maltose (99%), D-fructose (99%), α-lactose (99%), epinephrine (95%) and iron (II) chloride tetrahydrate (99%) were purchased from Sigma Aldrich (St. Louis, Missouri, USA). Sodium acetate trihydrate (99%) was purchased from Merck (Madison, Wisconsin, Milwaukee, USA). Monosodium phosphate monohydrate (99%) and disodium phosphate heptahydrate (99%) were purchased from J. T. Baker (Phillipsburg, New Jersey, USA) and Janssen Chimica (Geel, Belgium), respectively. Horse radish peroxidase (HRP) was purchased from

TCI (Tokyo, Japan). Ultrapure water was obtained using a Milli-Q ultrapure (18.2 MΩ-cm) system.

2.2.2 Preparation of Te NWs.
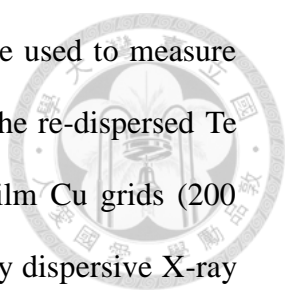
Hydrazine (10 mL) was added slowly to a beaker containing tellurium dioxide (0.016 g) under constant magnetic stirring at room temperature. The solution changed color from colorless to blue after 120 min, indicating the formation of Te NWs (average length: 785 nm; average diameter: 16 nm). To terminate the reaction and stabilize the Te NWs, the mixture was diluted 10-fold with CTAB (10 mM).

2.2.3 Synthesis of FeTe NRs.

Prior to use in the preparation of FeTe NRs, the as-prepared Te NWs was subjected to a centrifugation/wash cycle to remove most of the matrix (e.g., hydrazine). In a typical process for the synthesis of FeTe NRs, the Te NW pellet was re-dispersed in 10 mM CTAB. After 10 min, $FeCl_{3(aq)}$ (final concentration: 10 mM) was added to the mixture, which was then left at 60 °C for 1 h. The solution changed color from blue to yellow, indicating the formation of FeTe NRs. Then the FeTe NRs were subjected to three centrifugation/wash cycles to remove most of the matrices. Centrifugation was conducted at 15000 rpm for 10 min and ultrapure water (100 mL × 3) was used to wash the pellets. The pellets (FeTe NRs) were dried in air at ambient temperature (25 °C) prior to characterization and catalytic tests.

2.2.4 Characterization.

A double-beam UV−Vis spectrophotometer (Cintra 10e, GBC) was used to measure the absorption spectra of the Te NWs and FeTe NRs. JEOL JSM-1230 and

FEI Tecnai-G2-F20 transmission electron microscopes (TEM) were used to measure the sizes and shapes of the as-prepared Te NWs and FeTe NRs. The re-dispersed Te NWs and FeTe NRs were separately placed on formvar/carbon film Cu grids (200 mesh; Agar Scientific) and dried at ambient temperature. An energy dispersive X-ray (EDAX) system (Inca Energy 200, Oxford) was used to determine the composition of the as-prepared NMs. Raman spectra were recorded using a Raman spectrometer (Dong Woo 500i, Korea) equipped with a 50× objective and a charge-coupled detector. The excitation wavelength was 532 nm and the spectral aperture was 50 μm. The signal collection time for each sample was 30 s. Fluorescence spectra were recorded using Cary Eclipse Spectrophotometer equipped with a Xenon lamp.

2.2.5 H_2O_2 Detection through Peroxidase Mimics of FeTe NRs and Fe_3O_4 NPs.

To explore the possibility of using FeTe NRs as peroxidase mimics, the catalytic oxidation of the peroxidase substrate ABTS in the presence of H_2O_2 was tested. In short, ABTS (60 mM, 24 μL), FeTe NRs and Fe_3O_4 NPs (2.17 mg/mL, 10 μL), and different amounts of H_2O_2 (final concentrations 0.1–200 μM) were added into an acetate buffer solution (0.2 M, pH 4.0, 185 μL). The mixture was incubated at 30 ℃ for 10 min, and then the FeTe NRs and Fe_3O_4 NPs were removed through centrifugation at 15000 rpm for 10 min. The supernatant was diluted by a factor of 10 with water prior to absorption measurement. In order to investigate the influence of incubation temperature on the catalytic activity of FeTe NRs and Fe_3O_4 NPs, reactions were conducted at various temperatures (20–60 ℃). We also studied catalytic reactions over a pH range 2.0–12.0 in acetate solutions (0.2 M). The activity of HRP (40 mM, 10 μL) toward ABTS in the presence of H_2O_2 at an optimized condition (30 ℃, pH 7.0) was investigated.

2.2.6 Detection of Released Fe^{2+} Ions from FeTe NRs and Fe_3O_4 NPs.

A ferrous stock solution (10 mM) was prepared by dissolving iron (II) chloride in diluted hydrochloric acid solution (20 mM, 50 ml). The stock solution was used to prepare diluted standard Fe^{2+} solutions (0.5–100 μM) by appropriate dilution with 20 mM hydrochloric acid solution. FITC solution (0.1 mM) was prepared by dissolving the necessary weight of FITC in ethanol, which was then diluted with water to 1 μM. An iodine solution (0.3 μM) in ethanol was freshly prepared every time. To each 1.5-ml vial, FITC solution (1 μM, 100 μL), 600 μL of phosphate buffer solution (10 mM, pH 6.4), and standard Fe^{2+} solution (0.5–100 μM) were added to. To each of the mixture, iodine solution (0.3 μM, 90 μL) was added before dilution with ultrapure water (0.690 mL). The fluorescence intensity was then measured against a reagent blank at 515 nm with excitation at the wavelength 485 nm. The concentrations of the released Fe^{2+} ions from the FeTe NRs and Fe_3O_4 NPs were measured in a similar way to that for the standard Fe^{2+} solutions.

2.2.7 Detection of Glucose.

Phosphate buffered saline (PBS, 220 μL, 10 mM, pH 7.0) solutions containing glucose (1–500 μM) and GOx (6 μM) were incubated at 37 °C for 30 min. To the solutions, ABTS (60 mM, 24 μL), FeTe NRs stock solution (10 μL), and acetate buffer (0.2 M, pH 4.0, 800 μL) were added into. After each of the mixtures was incubated at 30 ºC for 10 min, the FeTe NRs were removed through centrifugation at 15000 rpm for 10 min. Each of the supernatant was diluted 10 times with water prior to absorption measurement. To investigate the specificity of the present assay, 5-mM maltose, fructose, lactose, dopamine, epinephrine and ascorbic acid instead of glucose were used as controls.

2.2.8 Detection of Glucose in Blood Samples.

20 µL plasma was mixed with 10 µL acetonitrile, which was then diluted a hundred fold with ultrapure water prior to centrifugation. Aliquots (20 µL) of the pretreated plasma solution (supernatant) were then spiked with a standard glucose solution (20 µL; 10 to 90 µM). The spiked samples were then subjected to the detection of glucose by applying the present assay. This was followed by comparing the results obtained from conducting a commercial blood glucose electrochemical approach (Abbott Laboratories, Alameda, CA, USA).

2.3 Results and Discussion

2.3.1 Characterization of FeTe NRs.
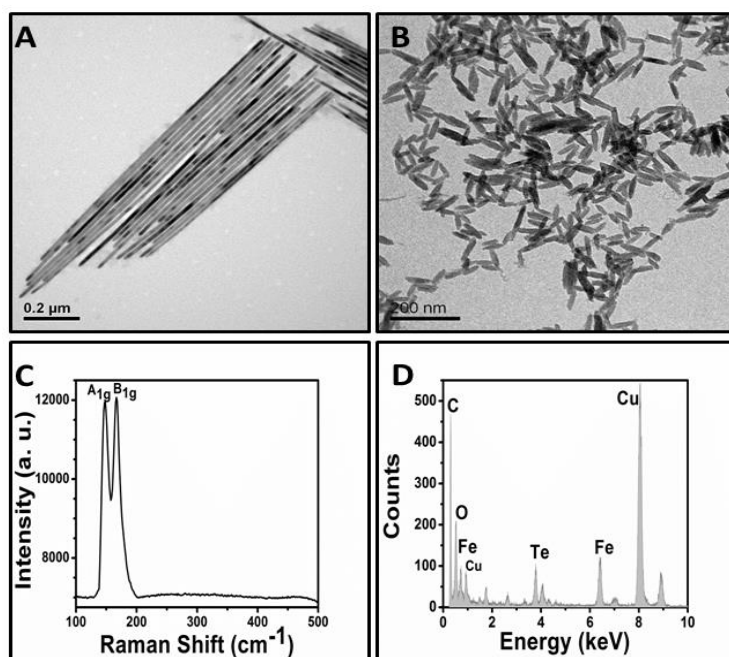
Fig. 2.1 Characterization of the as-synthesized Te NWs and FeTe NRs. (A) and (B) TEM image of Te NWs and FeTe NRs, respectively. (C) Raman and (D) EDAX spectra of FeTe NRs.

The lengths of the as-prepared Te NWs and FeTe NRs were estimated from

their corresponding TEM images (each 100 counts) to be (785 ± 170) and (45 ± 11) nm, respectively (Fig. 2.1A). The width of FeTe NRs (Fig. 2.1B) in the middle section is close to that of Te NWs (13.3 ± 1.8) nm vs. (16.2 ± 3.1) nm). The Raman scattering spectrum of the as-prepared FeTe NRs (Fig. 2.1C) reveals characteristic FeTe Raman active modes of A_{1g} (Te) and B_{1g} (Fe) at 148 and 168 cm^{-1}, respectively.[20] In comparison, the Raman peaks of pure Te NWs are known to be at 46, 62 and 182 cm^{-1}.[21] The detection of Te and Fe in the EDAX spectrum (Fig. 2.1D) further confirms the formation of FeTe NRs. FeTe NRs were formed through a galvanic reaction between Te and Fe^{3+} ions by (equation 1)

$$7Te + 18OH^- + 4Fe^{3+} \rightarrow 3TeO_3^{2-} + 4FeTe + 9H_2O \qquad (1)$$

Similar to that in the preparation of Au NRs,[14, 15] CTAB prefers binding to the {110} facet, leading to the anisotropic growth of FeTe seeds to form FeTe NRs. In addition, the CTAB bilayers on the surfaces of the FeTe NRs further stabilize them. The formation of FeTe NRs became apparent after a reaction time period of 20 min at 60 °C. To evaluate the practical potential of as-prepared FeTe NRs, we determined the peroxidase-like activity of the as-prepared FeTe NRs; FeTe NRs catalyze the reaction of H_2O_2 with peroxidase substrate ABTS (equation 2). Because the amount of the colored oxidized product of ABTS (λ_{max} = 418 nm) produced is proportional to the concentration of H_2O_2 present in the solution, the concentration of H_2O_2 can be determined by recording the absorbance at 418 nm of the solution according to the Beer's law

$$H_2O_2 + ABTS \xrightarrow{\text{FeTe NRs}} 2H_2O + \text{Oxidized ABTS.} \qquad (2)$$
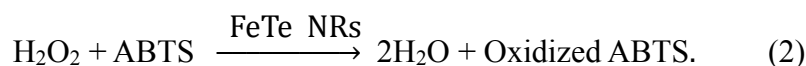
The as-prepared FeTe NRs (Fig. 2.2) provided about 9-fold absorbance value at 418 nm of that in the absence of the FeTe NRs.
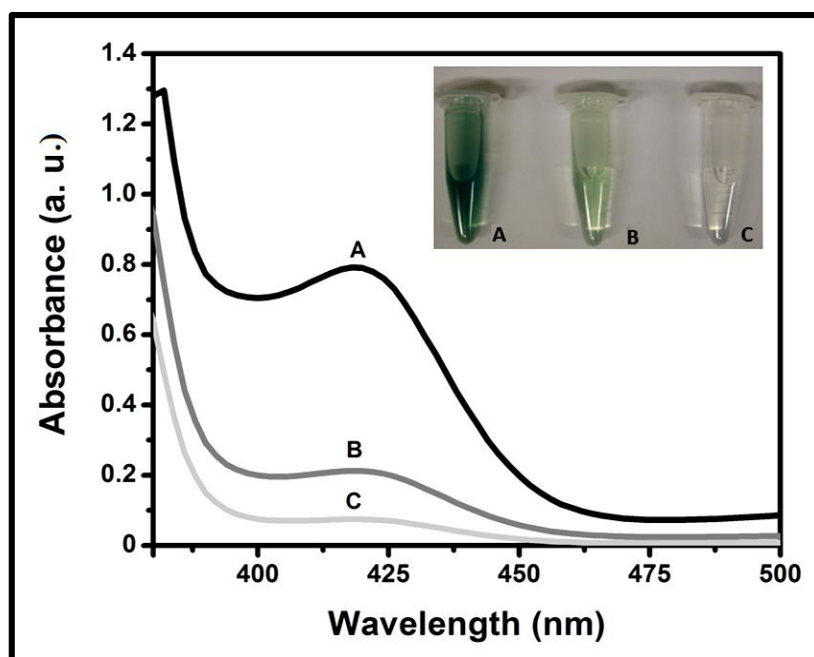
Fig. 2.2 Absorption spectra of solutions containing ABTS and H_2O_2 in the presence of (A) FeTe NRs (B) Fe_3O_4 NPs and (C) ABTS solution as a control. Inset: Photograph (from left to right: FeTe NRs, Fe_3O_4 NPs, and control). Concentrations: ABTS (60 mM), H_2O_2 (100 mM), Fe_3O_4 NPs (2.17 mg/ml), and FeTe NRs (2.17 mg/ml). Acetate buffer: (0.2 M, pH 4.0).

Under these studied conditions, the catalytic activity of the FeTe NRs was higher than that of the Fe_3O_4 NPs.[8] The catalytic activity of Fe_3O_4 NPs is dependent on the solution pH and reaction temperature.[7, 8] Thus, the pH- and temperature-dependent activities of the FeTe NRs and Fe_3O_4 NPs were investigated in the current study. Fig. 2.3 shows the response curves in acetate buffer solutions (0.2 M) containing 100 μM H_2O_2 over a pH range (2.0–12.0) at 30 °C. In the absence of any NMs, the absorbance decreased gradually from pH values 2.0 to 5.0 and almost no reaction was observed at pH values higher than 5.0. Decomposition (hydrolysis) of H_2O_2 tends to occur rapidly at a pH higher than 5.0, leading to loss of its oxidation

activity toward ABTS.[22-24] Similar trends occurred in the presence of the FeTe NRs and Fe_3O_4 NPs.
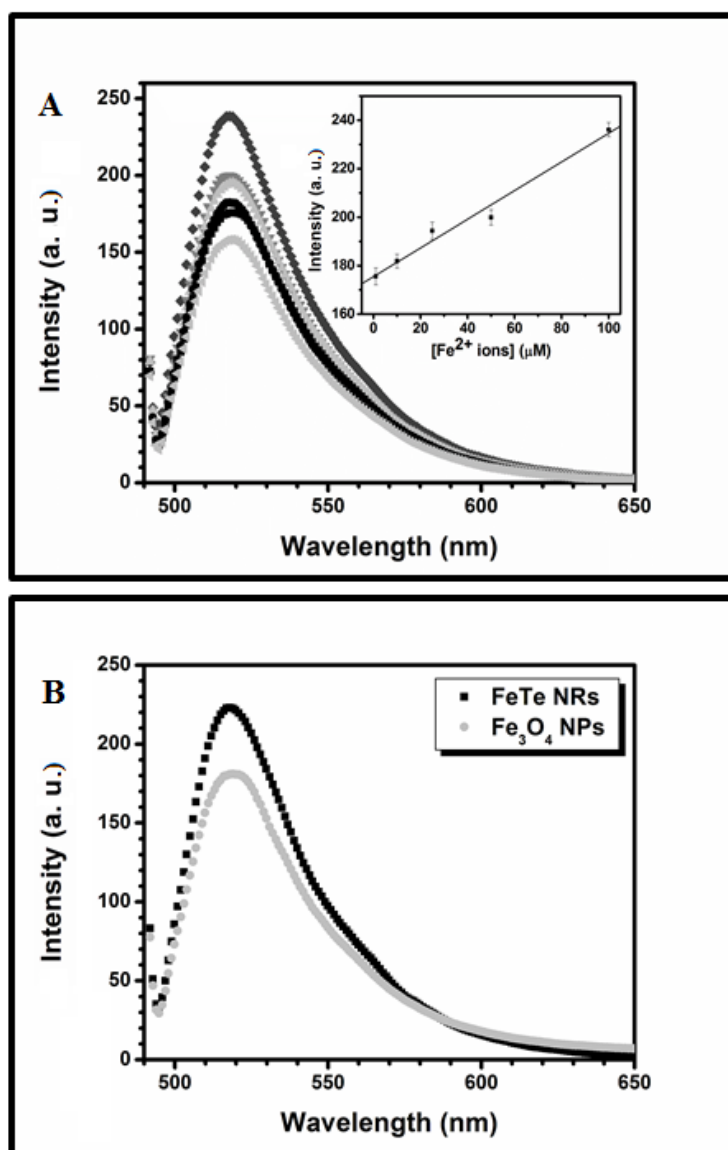
Fig. 2.3 Fluorescence spectra of FITC (0.1 mM) in the presence of (A) various concentrations of Fe^{2+} ions and (B) FeTe NRs and Fe_3O_4 NPs at 30 °C. (A) FITC concentrations range from 0.5 to 100 μM. Inset is the linear range from 1 to 100 μM. Concentrations: Iodine solution (0.3 μM), Phosphate buffer: (10 mM, pH 6.4).

In addition to instability of H_2O_2 at high pH values, no sufficient amount of

Fe^{2+} ions available in the systems also accounts for their low activity.[25, 26] We note that the solubility product of $Fe(OH)_3$ is $(2.6 \pm 0.2) \times 10^{-39}$.[27] Maximum difference in the absorbance values in the presence and absence of the FeTe NRs and Fe_3O_4 NPs occurred at pH 4.0 and 3.0, respectively. Both in the absence and presence of the FeTe NRs and Fe_3O_4 NPs, the absorbance increased when the reaction temperatures were raised from 20 to 60 ℃. We plotted the differential absorbance (ΔA) values against reaction temperature, in which $\Delta A = A_{418\,nm}$ (FeTe NRs or Fe_3O_4 NPs) $- A_{418\,nm}$ (no NMs) (inset). 30 ℃ and 45 ℃, respectively. The maximum values for the FeTe NRs and Fe_3O_4 NPs occurred at 30 ℃ and 45 ℃, respectively. This is because the released Fe^{2+} ions from FeTe NRs reached a maximum value at 30 ℃ (Fig. 2.3B).

2.3.2 Detection of H_2O_2.

The catalytic activity of FeTe NRs toward ABTS oxidation is proportional to the amount of released Fe^{2+} ions. However, in the case of Fe_3O_4 NPs, the temperature for the generation of a maximum amount of Fe^{2+} ions occurred at 45 ℃. The difference in temperature reaching maximum amounts of Fe^{2+} ions released is mainly because the bond strength of Fe with O is stronger in Fe_3O_4 than that with Te in FeTe.[28]

It has been shown that the Fe^{2+} ions released from Fe_3O_4 NPs play a dominant role in the catalytic ABTS oxidation with H_2O_2.[7, 8] To prove it, we determined the concentration of Fe^{2+} ions released from the FeTe NRs and Fe_3O_4 NPs using FITC as a fluorophore (Fig. 2.3).[29] The amount of Fe^{2+} ions released from the FeTe NRs was found to be one order in magnitude higher than that released from the Fe_3O_4 NPs. This leads to a plausible explanation of the greater enhancement in the absorbance observed when using the FeTe NRs than using the Fe_3O_4 NPs.
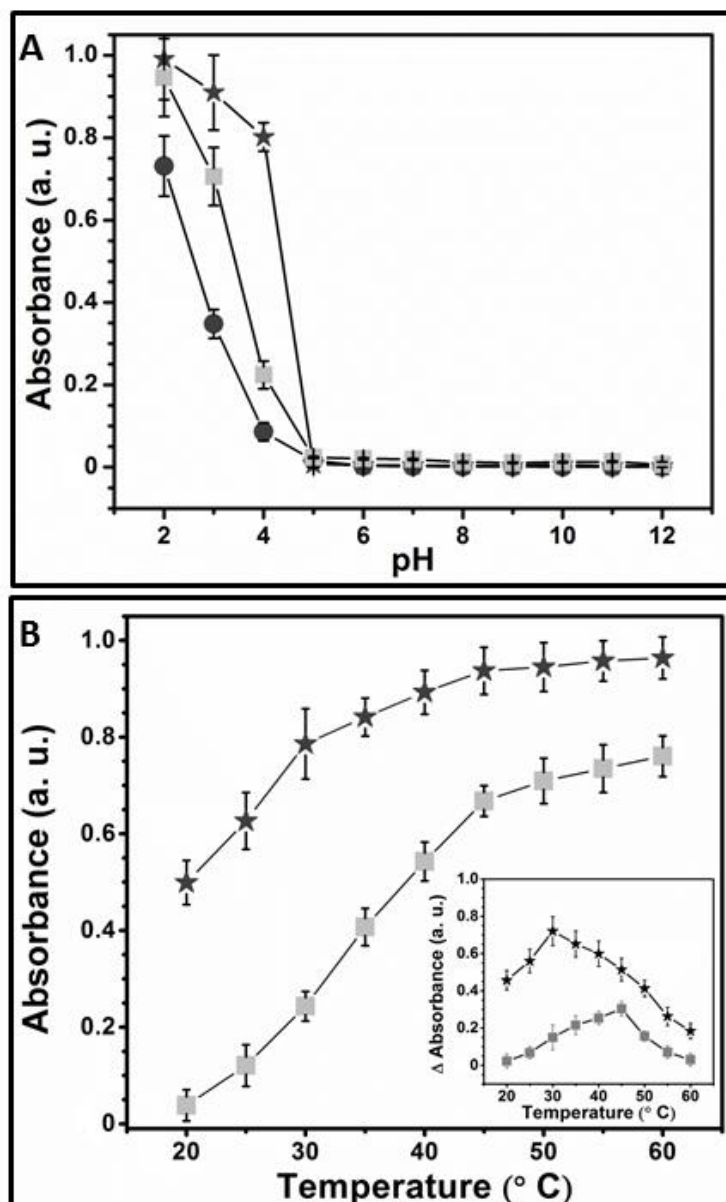
Fig. 2.4 Effects of pH and temperature on the catalytic activity of the Fe$_3$O$_4$ NPs and FeTe NRs for H$_2$O$_2$-mediated ABTS reaction. (A) pH and (B) temperature dependent response curves: ⋆ for FeTe NRs, ■ for Fe$_3$O$_4$ NPs, and ● for the control. Inset to (B) ΔA against temperature, where ΔA = A$_{418 \text{ nm}}$ (FeTe NRs or Fe$_3$O$_4$ NPs) − A$_{418 \text{ nm}}$ (Blank).
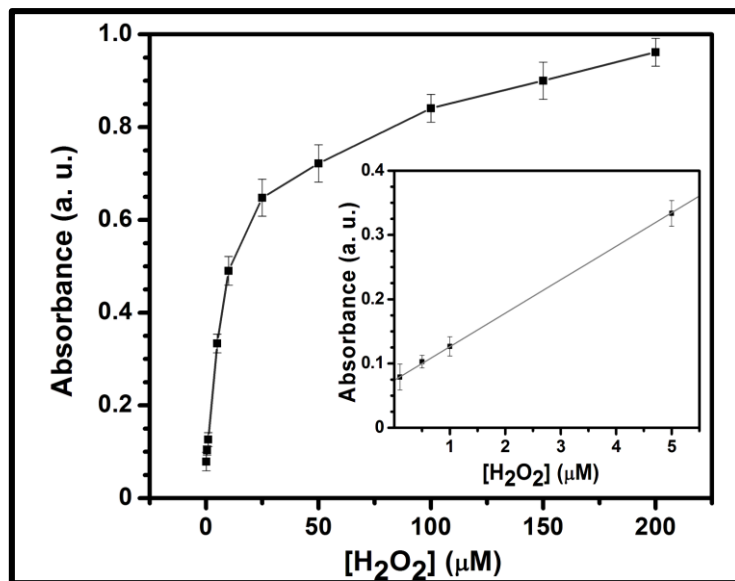
Fig. 2.5 A dose-response curve for H_2O_2 detection when using FeTe NRs. Inset: linearity of absorbance against H_2O_2 concentration ranging over 0.1–5 μM.

The optimum pH and temperature are 4.0 (0.2 M acetate buffer) and 30 ℃, respectively (Fig. 2.3). Under these conditions, we determined the effect of H_2O_2 on the absorbance of the solutions containing the FeTe NRs and ABTS. The Fig. 2.5 displays the increase in absorbance upon increasing the H_2O_2 concentration. A linear relationship (inset to Fig. 2.5) between the absorbance and the H_2O_2 concentration ranging from 0.1 to 5 μM (R^2 = 0.99) was obtained, with a limit of detection at a signal-to-noise ratio of 3 of 55 nM. The LOD provided by using the FeTe NRs is two orders in magnitude lower than that provided by the Fe_3O_4 NPs.[8] Relative to HRP,[7] the FeTe NRs provided at least 150 fold higher sensitivity.

2.3.3 Glucose Detection through Enzyme Mimics of FeTe NRs.

Coupling the catalytic reaction shown in equation 2 with the glucose catalytic reaction by GOx (equation 3), colorimetric detection of glucose can be readily

realized.

$$O_2 + \text{Glucose} \xrightarrow{\text{GOx}} H_2O_2 + \text{Gluconic acid} \qquad (3)$$
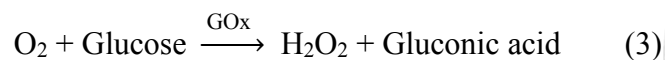
The two reactions (2 and 3) were carried out separately as the optimal pH values for the enzyme reaction and the mimetic reaction were at 7.0 and 4.0 respectively.[8] The H_2O_2 produced in equation (3) reacted subsequently with ABTS that was catalyzed by FeTe NRs as shown in equation (2). The increase in absorbance correlates with the glucose concentration (Fig. 2.6A).
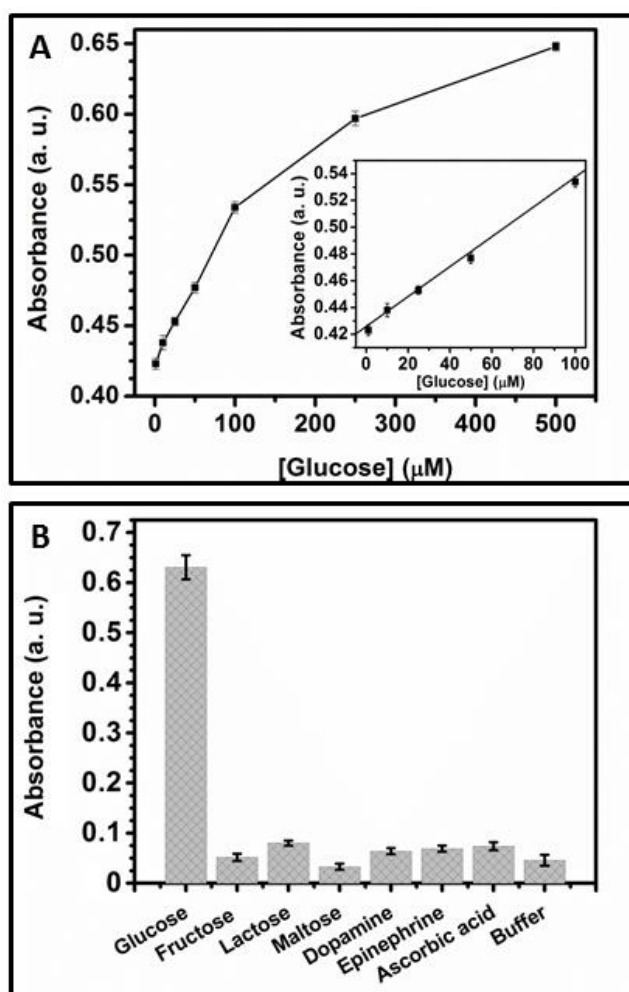
Fig. 2.6 (A) Sensitivity and (B) selectivity of the assay using GOx and FeTe NRs for the detection of glucose. Concentrations of solutes are 500 µM for glucose and 5 mM for the other common interfering species. Inset to (A): linearity of absorbance against glucose concentration range over 1−100 µM.

The absorbance against the concentration of glucose is linear (inset to Fig. 2.6A) in the range of 1–100 µM ($R^2 = 0.99$), with an LOD of 0.38 µM. The LOD provided by FeTe NRs is two orders in magnitude lower than that provided by Fe_3O_4 NPs.[8] Control experiments were carried out to test the specificity of the developed system by using fructose, lactose, maltose, dopamine, epinephrine and ascorbic acid all at a concentration of 5 mM instead of glucose (Fig. 2.6B).

2.3.4 Practicality

When compared to electrochemical biosensors,[30-32] the FeTe NRs-based sensing system shows comparable sensitivity and selectivity for glucose. With the advantages of sensitivity and selectivity, we used the FeTe NRs to determine the concentration of glucose in plasma. Values higher or lower than the reference (3.6–6.0 mM) are of diagnostic significance.[33] We determined the concentration of glucose in the spiked blood samples, with a linear plot of the absorbance (Y) against the glucose concentration (X); 0.5120 = 0.0009X + 0.4483. We calculated the glucose concentration to be (7.07 ± 0.16) mM (n = 5) using the above equation and dilution factor. The concentration of glucose in the blood sample was (7.33 ± 0.09) mM when using a commercial blood glucose electrochemical approach. The F-test and t-test values were 1.98 and 2.30 respectively for the FeTe NR assay ($n = 5$) at a 95% confidence level, revealing that the two methods provided no different results.

2.4 Conclusions

FeTe NRs were synthesized form Te NWs through a galvanic reaction. The as-prepared FeTe had a higher enzyme activity toward H_2O_2-mediated ABTS reaction than those of HRP and Fe_3O_4 NPs. We have found that the catalytic activity of FeTe is
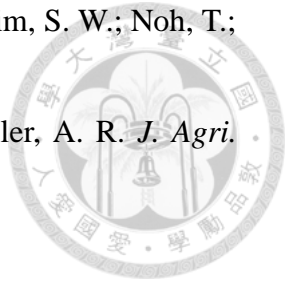
dependent on the amounts of Fe(II) ions on their surfaces, pH and temperature. When using GOx and the FeTe NRs, the assay (pH 4.0, 30 ºC) provided high sensitivity (55 nM) and selectivity for the detection of glucose. The present assay was validated by the detection of glucose in plasma, showing advantages of simplicity, accuracy, and rapidity. This opens up the possibility of using FeTe NRs as enzyme mimics for the detection of various analytes of interest when suitable enzymes are used to generate H_2O_2.

References
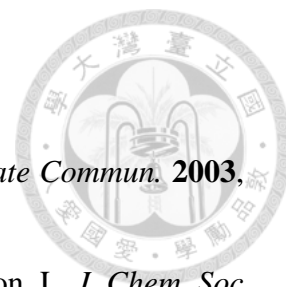
(1) Tanaka, A.; Takeda, Y.; Nagasawa, T.; Takahashi. K. *Solid State Commun.* **2003**, *126*, 191-196.

(2) McNeillie, A.; Brown, D. H.; Smith, W. E.; Gibson, M.; Watson, L. *J. Chem. Soc. Dalton Trans.* **1980**, *5*, 767-770.

(3) Duff, D. G.; Baiker, A.; Edwards, P. P. *Langmuir* **1993**, *9*, 2301-2309.

(4) Liu, G.; Lin, Y. *Electrochem. Commun.* **2006**, *8*, 251-256

(5) Dickinson, B. C.; Chang, C. J. *J. Am. Chem. Soc.* **2008**, *130*, 9638-9639.

(6) Zhou, M.; Dong, S. *Acc. Chem. Res.* **2011**, *44*, 1232-1243.

(7) Gao, L.; Zhuang, J.; Nie, L.; Zhang, J.; Zhang, Y.; Gu ,N.; Wang, T.; Feng, J.; Yang, D.; Perrett, S.; Yan, X. *Nat Nano.* **2007**, *2*, 577-583.

(8) Wei, H.; Wang, E. *Anal. Chem.* **2008**, *80*, 2250-2254.

(9) Song, Y.; Wang, X.; Zhao, C.; Qu, K.; Ren, J.; Qu, X. *Chem.-Eur. J.* **2010**, *16*, 3617-3621.

(10) Wang, X.-X.; Wu, Q.; Shan, Z.; Huang, Q.-M. *Biosens. Bioelectron.* **2011**, *26*, 3614-3619.

(11) Jv, Y.; Li, B.; Cao, R. *Chem. Commun.* **2010**, *46*, 8017-8019.

(12) Randolph, L. M.; Chien, M.-P.; Gianneschi, N. C. *Chem. Sci.* **2012**, *3*, 1363-1380

(13) Larmour, I. A.; Faulds, K.; Graham, D. *Chem. Sci.* **2010**, *1*, 151-160.

(14) Lin, Z.-H.; Yang, Z.; Chang, H.-T. *Cryst. Growth Des.* **2007**, *8*, 351-357.

(15) Lin, Z.-H.; Chang, H.-T. *Langmuir*, **2007**, *24*, 365-367

(16) Lin, Z.-H.; Lin, Y.-W.; Lee, K.-H. Chang, H.-T. *J. Mater. Chem.* **2008**, *18*, 2569-2572.

(17) Lin, Z.-H.; Lin, M.-H.; Chang, H.-T. *Chem.-Eur. J.* **2009**, *15*, 4656-4662.

(18) Mizuguchi, Y.; Tomioka, F.; Tsuda, S.; Yamaguchi, T.; Takano, Y. *Appl. Phs. Lett*, **2009**, *94*, 012503-1 - 012503-3.

(19) Hsu, F.-C.; Luo, J.-Y.; Yeh, K.-W.; Chen, T.-K.; Huang, T.-W.; Wu, P. M.; Lee, Y.-C.; Huang, Y.-L.; Chu, Y.-Y.; Yan, D.-C.; Wu, M.-K. *Proc. Natl. Acad. Sci.* **2008**, *105*, 14262-14264.

(20) Xia, T. L.; Hou, D.; Zhao, S. C.; Zhang, A. M.; Chen, G. F.; Luo, J. L.; Wang, N. L.; Wei, J. H.; Lu, Z. Y.; Zhang, Q. M. *Phys. Rev. B.* **2009**, 79, 140510-1 - 140510-4.

(21) Song, H.; Cho, K.; Kim, H.; Lee, J. S.; Min, B.; Kim, H. S.; Kim, S. W.; Noh, T.; Kim, S. *J. Cryst. Growth*, **2004**, *269*, 3617-3621.

(22) Ozgen, M.; Reese, R. N.; Tulio, A. Z.; Scheerens, J. C.; Miller, A. R. *J. Agri. Food Chem.* **2006**, *54*, 1151-1157.

(23) Nicoll, W. D.; Smith, A. F.; *Ind. Eng. Chem.* **1955**, *47*, 2548.

(24) Gogate, P. R.; Pandit, A. B. *Adv. Environ Res*. **2004**, *8*, 553-597.

(25) Hsueh, C. L.; Huang, Y. H.; Wang, C. C.; Chen, C. Y. *Chemosphere*, **2005**, *58*, 1409-1414.

(26) Tekin, H.; Bilkay, O.; Ataberk, S. S.; Balta, T. H.; Ceribasi, I. H.; Sanin, F. D.; Dilek, F. B.; Yetis, U. *J. Hazard. Mater.* **2006**, *136*, 258-265.

(27) Meighan, J. MacNeil, M.; Falconer, R. *J. Chem. Educ.* **2008**, *85*, 254-255.

(28) Aramu, F.; Manca, P. *Nuovo Cim.* **1964**, *33*, 1025-1030.

(29) Zhu, G. H.; Zhu, Z. C.; Qiu, L. F. *Anal. Sci.* **2002**, *18*, 1059-1061.

(30) Wang, J. *Chem. Rev*. **2007**, *108*, 814-825.

(31) Li, Y.; Lin, X. *Sensor Actuat. B*, **2006**, *115*, 134-139.

(32) Wang, J. *Electroanal*. **2005**, *17*, 1341–1346.

(33) Garg, A.; Bonanome, A.; Grundy, S. M.; Zhang, Z.-J.; Unger, R. H. *N. Engl. J. Med.* **1988**, *319*, 829-834.
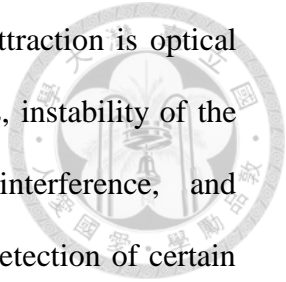
Chapter 3

Iron Telluride Nanorods-Based System for the Detection of Total Mercury in Blood

3.1 Introduction

Mercury is a severe pollutant that has a substantial bearing on the ecosystem because it is non-biodegradable, bio-accumulative and highly mobile.[1] Mercuric ion (Hg^{2+}) is one of the most stable inorganic forms of mercury, which can damage the brain, heart, kidney, stomach, and intestines even at very low concentrations.[2] When coming from industrial sources it gets converted into its highly toxic organic forms such as methyl mercury (CH_3Hg^+) and ethyl mercury ($C_2H_5Hg^+$), which may end up in agricultural and food products. Dental amalgams have been another potential source of mercury accumulation into the blood stream, but the possible risk associated with vaccines such as thimerosal is a much newer concern.[1] The Environmental Protection Agency (EPA) in the United States sets allowable or safe daily intake of methyl mercury to be less than 0.1 μg of mercury per kilogram per day.[2] Normal concentrations of total whole blood Hg are typically less than 5.0 μg L^{-1} (24.4 nM) in adults,[3] but recent data in the non-institutionalized US population show that the concentrations of whole blood Hg is 7.1 μg L^{-1} for most adult females.[4]

Atomic spectrometric techniques such as cold vapor atomic absorption spectroscopy have been primarily used for the detection of mercury in biological samples.[3-5] However, biological, organic residues may cause blockages within the microwave reaction coil and back pressure within the flow-injection manifold as a result of exothermic reactions occurring within the microwave cavity.[6] Inductively coupled plasma mass spectrometry (ICP-MS) has become more popular for the detection of mercury in biological samples, mainly because they relative to most atomic spectrometric techniques provide lower detection limits and wider dynamic ranges.[7-9] However for point-of-use applications, they are rather complicated and time-consuming for sample preparation as well as require expensive and sophisticated

instrumentation and noble gas. Another method that has gained attraction is optical detection of Hg^{2+} ions using organic ionophores. [10-15] Nevertheless, instability of the probe, cross-sensitivity toward other metal ions, matrix interference, and photobleaching may occur. In addition, the probes usually allow detection of certain Hg species (not total amount). Gold as well as silver nanoparticles (Au, Ag NPs) and cadmium sulfide (CdS) quantum dots (QDs) have been used for the detection of mercury through optical and electrochemical techniques.[16-19] Although they are sensitive, use of expensive Au^{3+}, Ag^{2+} ions, and potentially toxic Cd^{2+} ions are concerns, respectively. The aim of this study is to prepare low-cost FeTe NRs for the determination of total concentration of mercury species. The FeTe NRs interacted specifically with Hg^{2+} ions to release Fe^{2+} ions that catalyzed the oxidation of 2,2'-azino-bis(3-ethylbenzo-thiazoline-6-sulfonic acid) diammonium salt (ABTS) with H_2O_2. We investigated the effects of pH, temperature, solvent effect and reaction time on the sensitivity of this approach toward Hg^{2+}. Practicality of the present detection system was validated by the determination of the concentration of mercury in blood samples obtained from National Institute of Standards and Technology (NIST).

3.2 Experimental Section

3.2.1 Materials

SDS (99%) and hexadecyltrimethylammonium bromide (CTAB, $C_{19}H_{42}NBr$, 99%) were obtained from Acros. Sodium tetrachloroaurate dihydrate ($NaAuCl_4 \cdot 2H_2O$) was obtained from Aldrich. Rhodamine 6G (R6G, $C_{28}H_{31}N_2O_3Cl$, 99%) was obtained from Sigma. Tellurium dioxide (99.9%) and hydrazine monohydrate (80%) were purchased from SHOWA (Tokyo, Japan). Deionized water from a Milli-Q ultrapure

(18.2 MΩ-cm) system was used in this study.

3.2.2 Synthesis of Te NWs
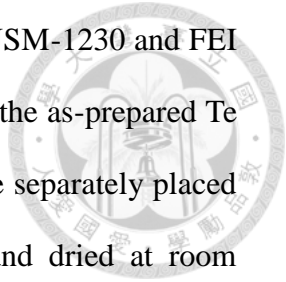
Te NWs were prepared from the reduction of TeO_2 with N_2H_4. Typically, tellurium dioxide (16 mg) was added slowly to hydrazine monohydrate (10 mL) in a beaker at room temperature under constant magnetic stirring. The solution sequentially changed color from colorless to blue after 1 h. The blue color indicated the formation of Te MWs. To terminate the reactions, the solutions were diluted 10-fold with SDS solution (10 mM).

3.2.3 Preparation of FeTe NRs

The as-prepared Te NWs were subjected to centrifugation [relative centrifugation force (RCF): 25,000 g for 10 min] and washed (10 mL of water) to remove most of the matrix (e.g., hydrazine). In a typical process for the synthesis of FeTe NRs, the Te NW pellet (ca. 30 mg) was re-dispersed in CTAB (9 mL, 10 mM). After 10 min, $FeCl_{3(aq)}$ (1 mL, final concentration: 10 mM) was added to the mixture, which was then left at 60 °C for 1 h.[39] The solution changed color from blue to yellow, indicating the formation of FeTe NRs. Then the FeTe NRs were subjected to three centrifugation/wash cycles to remove most of the matrices. Centrifugation was conducted at RCF 12,000 g for 10 min and ultrapure water (10 mL × 3) was used to wash the pellet. The pellets (FeTe NRs) were dried in air at ambient temperature (25 °C) prior to characterization and catalytic tests.

3.2.4 Characterization

A double-beam UV–vis spectrophotometer (Cintra 10e, GBC) was used to

record the absorption spectra of the Te NWs and FeTe NRs. JEOL JSM-1230 and FEI Tecnai-G2-F20 TEM were used to measure the sizes and shapes of the as-prepared Te NWs and FeTe NRs. The re-dispersed Te NWs and FeTe NRs were separately placed on formvar/carbon film Cu grids (200 mesh; Agar Scientific) and dried at room temperature. An energy dispersive X-ray (EDAX) system (Inca Energy 200, Oxford) was used to determine the composition of the as-prepared NMs. Raman spectra were recorded using a Raman spectrometer (Dong Woo 500i, Korea) equipped with a 50× objective and a charge-coupled detector. The excitation wavelength was 532 nm and the spectral aperture was 50 μm. The signal collection time for each sample was 30 s. ICP-MS for the determination of the concentrations of Fe^{2+} and Hg^{2+} ions in the HgTe and FeTe NRs was conducted using an Agilent Series 7700 ICP-MS system (Santa Clara, CA, USA).

3.2.5 Detection of Hg^{2+} ions using FeTe NRs

Aliquots (100 μL) of $HgCl_2$ solutions (final concentrations 5–500 nM) in phosphate solution (10 mM, pH 6.4) were separately added to FeTe NRs (50 μL, 250 nM) in phosphate solution (10 mM, pH 6.4). The effects of pH, temperature and reaction time on the detection of Hg^{2+} were investigated over the pH range 2.0–12.0, temperature range 30–75 °C, and reaction period 15–120 min, respectively. Under constant stirring at 60 ℃ for 90 min, the color changed from yellow to dark brown, indicating the formation of HgTe NRs. After centrifugation at 15,000 g for 10 min, the supernatants containing the released Fe^{2+} ions were collected and mixed with ABTS (60 mM, 24 μL), H_2O_2 (24 μL, 0.1 μM). The mixtures were subsequently mixed with acetate buffer solution (0.2 M, pH 4.0, 185 μL), which were incubated at 30 ℃ for 10 min. Each of the mixtures was diluted by a factor of 10 with water prior to absorption

measurement. To test the counter ion effect, $Hg(NO_3)_2$ and $Hg(CH_3COO)_2$ were used to replace $HgCl_2$. In order to evaluate the solvent effect, phosphate solution (10 mM, pH 6.4) containing 49% of methanol, ethanol, hexane or chloroform were used to prepare the mixture.
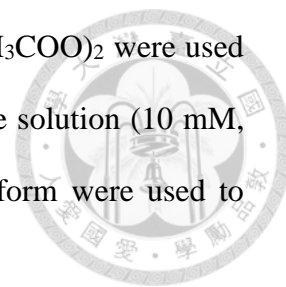
3.2.6 Determination of the concentrations of Hg^{2+} and Fe^{2+} ions using ICP-MS
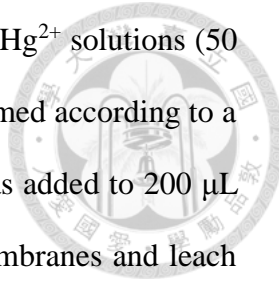
ICP-MS was used to determine the concentrations of metal ions in the products obtained upon the reaction of FeTe NRs (50 µL, 0.32 µg mL^{-1}) with Hg^{2+} ions (10–100 nM). The mixtures were subjected to three centrifugation/wash cycles. Centrifugation was conducted at RCF 12,000 g for 10 min and ultrapure water (10 mL × 3) was used to wash the pellets. The pellets were re-dispersed in HNO_3 solution (2%, 5mL) for the ICP-MS measurement. Standard solutions of $HgCl_2$ (final concentrations of 10–100 nM) and $FeCl_2$ (10–100 nM) were prepared in HNO_3 solution (2%, 5mL).

3.2.7 Detection of released Fe^{2+} ions upon formation of HgTe NRs.

The supernatants of the mixtures of FeTe NRs (1.25 µg mL^{-1}) and Hg^{2+} (5 - 500 nM) ions were placed in vials, in which   aliquots (600 µL) of phosphate buffers (10 mM, pH 6.4) and FITC in ethanol solution (final concentration: 1 µM, 100 µL) were added to. To each of the mixtures, iodine solution (0.3 µM, 90 µL) was added before dilution with ultrapure water (0.69 mL). The fluorescence intensity was then measured against a reagent blank at 515 nm with the excitation wavelength of 485 nm.

3.2.8 Detection of Hg^{2+} in blood

The blood sample (SRM 955c) was frozen at −20 °C prior to use. Aliquots of

the 2-fold diluted blood sample (50 μL) were spiked with standard Hg^{2+} solutions (50 μL, 3-18 nM). Acidic digestion of whole blood samples was performed according to a routine sample-digestion method. Briefly, HNO_3 (300 μL, 1 M) was added to 200 μL of whole blood and then left for 30 min to rupture the red cell membranes and leach Hg species. The insoluble material was removed through centrifugation twice (RCF: 10,000 g, 10 min). Acetonitrile (10 μL) was added subsequently to the supernatant and the mixture was centrifuged again (RCF: 10,000 g; 10 min). The supernatant was then heated at 90 °C for 1 h to evaporate most of the acid and acetonitrile. After cooling to room temperature, the solution was passed through a filter (cutoff 3 kDa; nominal pore size ca. 0.3 nm) and diluted to 2 mL with Tris-acetate buffer (5 mM, pH 7.0). FeTe NRs were added to the dilute solutions, which were subjected to heating at 60 °C for 90 min under constant stirring. This was followed by centrifugation at 15,000 g for 10 min. The supernatants containing the released Fe^{2+} ions were collected and mixed with ABTS (60 mM, 24 μL) and H_2O_2 (0.1 μM). The mixtures were subsequently mixed with acetate buffer solution (0.2 M, pH 4.0, 185 μL) and incubated at 30 ℃ for 10 min, afterwards diluted by a factor of 10 with water prior to absorption measurement.

3.3 Results and Discussion

3.3.1 Sensing mechanism

Scheme 3.1 shows the detection of Hg^{2+}, mainly through the cation exchange reaction between the Fe^{2+} ions in FeTe NRs and Hg^{2+} ions as shown in Equation (1), leading to the formation of HgTe nanostructures and consequently the release of Fe^{2+} ions.

$$FeTe + Hg^{2+} \rightarrow HgTe + Fe^{2+} \quad (1)$$

We note that the FeTe NRs were stable at 4 °C for at least 30 days. Although the solubility product of FeTe is unavailable from literature, the solubility product of FeTe is not much smaller than that of FeS (10^{-19}),[22, 23] which is much larger than that (10^{-70}) of HgTe. The released Fe^{2+} ions present in the supernatant catalyze the reaction of ABTS with H_2O_2 as shown in Equation (2).

$$H_2O_2 + ABTS \xrightarrow{\textbf{Fe}^{2+}} 2H_2O + \text{Oxidized ABTS} \qquad (2)$$
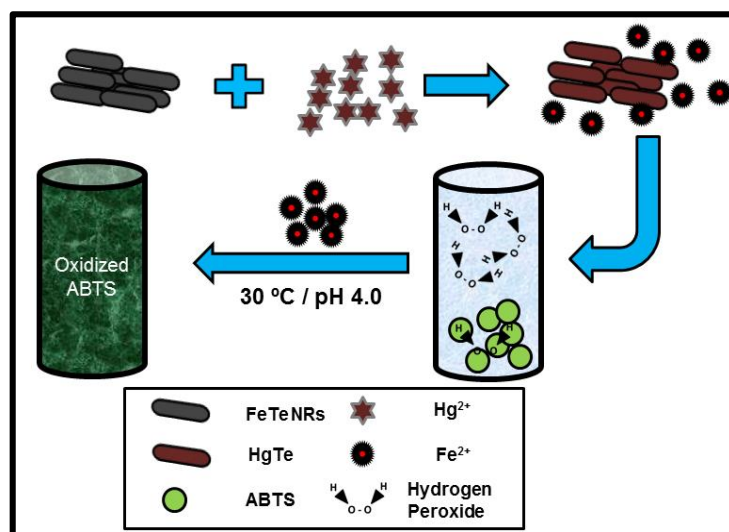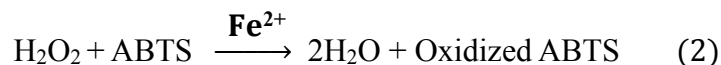
Scheme 3.1 Colorimetric detection of Hg^{2+} ions using FeTe NRs. Fe^{2+} ions released from the FeTe NRs mainly through the cation exchange reaction with Hg^{2+} ions catalyze the reaction of ABTS (60 mM) with H_2O_2 (0.1 μM).

The amount of ABTS product (formed is proportional to the concentration of Fe^{2+} ions and thus to that of the Hg^{2+} ions. We note that the oxidized product of ABTS has an absorption wavelength maximum at 418 nm. Thus, by using a calibration curve of the absorbance values at λ_{max} = 418 nm against the concentration of the Fe^{2+} ions in the standard solutions, the concentration of Fe^{2+} displaced and thus that of Hg^{2+} ions in the sample solution can be determined.
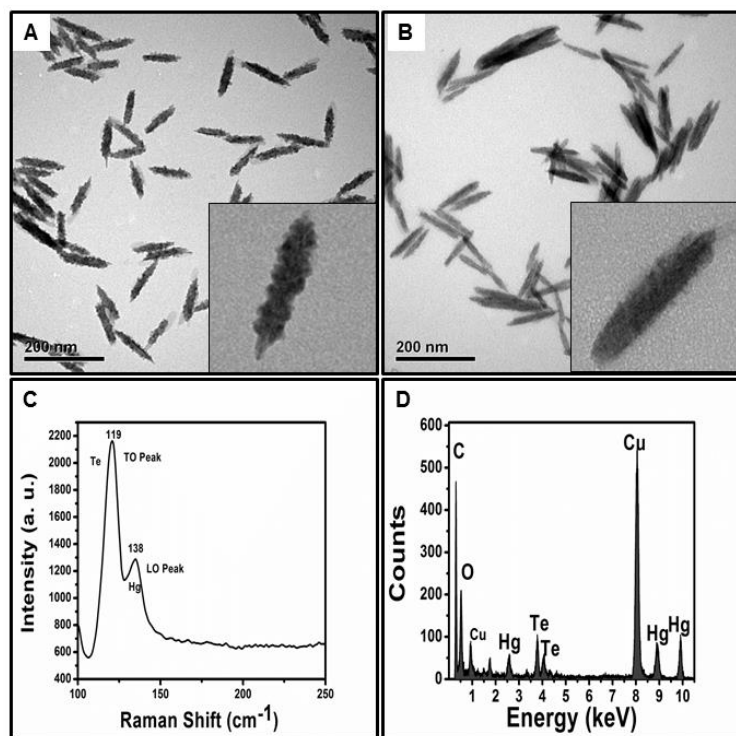
Fig. 3.1 Characterization of the synthesized FeTe and HgTe NRs. (A) and (B) TEM image of FeTe and HgTe NRs, respectively. (C) Raman and (D) EDAX spectra of the as-formed HgTe. The concentrations of FeTe and Hg^{2+} ions are 5 and 0.5 mM, respectively.

To support the formation of HgTe nanostructures from the reaction of FeTe NRs and Hg^{2+} ions, we conducted TEM, EDAX, and Raman measurements. The TEM image of the as-prepared FeTe NRs (Fig. 3.1A) is shown, with average length and width (the widest part) of (105 ± 21) and (19 ± 2) nm (100 counts), respectively. On the other hand, the TEM image of HgTe NRs depicted in Fig. 3.1B displays their average length and width were (112 ± 26) and (23 ± 8) nm, respectively. The HgTe NRs has a marginally larger lattice constant (6.458 Å) in comparison to that (6.26 Å) of the FeTe NRs.[24, 25] Moreover, the HgTe NRs relative to the FeTe NRs had a comparatively smoother surface. The Raman scattering spectrum of the HgTe NRs (Fig. 3.2C) reveals characteristic transverse optical (TO) and longitudinal optical (LO) peaks at 119 and 139 cm^{-1}, which are close to those (118 and 140 cm^{-1}, respectively)

for the bulk HgTe. In comparison, the Raman peaks of the Te NWs are at 46, 62 and 182 cm^{-1},[26] while those for the FeTe NRs are at 148 (A$_{1g}$) and 168 cm^{-1} (B$_{1g}$).[21] The EDAX pattern clearly show the Hg and Te signals (Fig. 3.1D), further confirming the complete replacement of Fe^{2+} ions by Hg^{2+} and the formation of HgTe NRs.
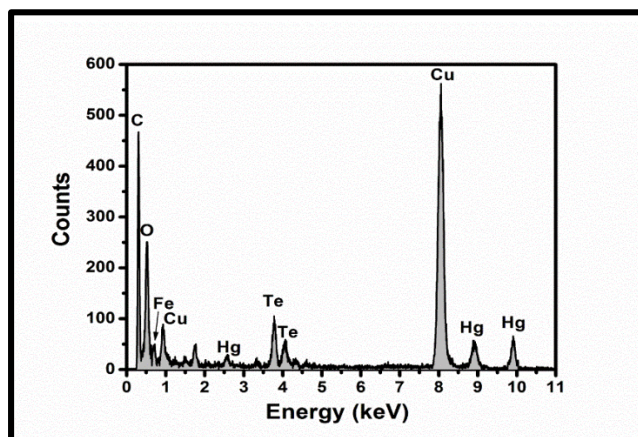
Fig. 3.2 EDAX spectrum of HgTe NRs displaying the displacement of Fe^{2+} ions by Hg^{2+} ions during the course (30 min) of the reaction
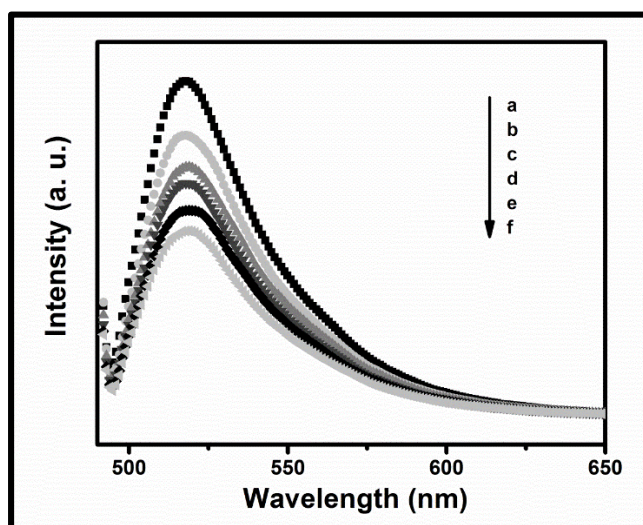
Fig. 3.3 Fluorescence spectra of FITC (1 μM) in the mixtures of FeTe NRs (1.25 μg mL^{-1}) and Hg^{2+} ions (a: 500, b: 250, c: 100, d: 50, e: 25, f: 5 nM). Mixtures were prepared in phosphate buffer (10 mM, pH 6.4) containing iodine (0.3 μM).

The Fe peak was still apparent in the FeTe NRs in intermediate steps (e.g. after the reaction for 30 min as depicted in Fig. 3.2). We also detected the

concentration of Fe^{2+} ions released by using FITC as a fluorophore. The fluorescence of FITC increased upon increasing the concentration of Fe^{2+} ions (Fig. 3.3), supporting the formation of Fe^{2+} ions between the reaction of FeTe NRs and Hg^{2+} ions. In addition, the Fe^{2+} ions released were stable in the acidic solution during the analysis.

3.3.2 Effect of reaction time, temperature, and pH

It is known that Fe^{2+} ions have the highest catalytic activity toward the reaction of ABTS with H_2O_2 at pH 4.0 (0.2 M acetate buffer).[21]
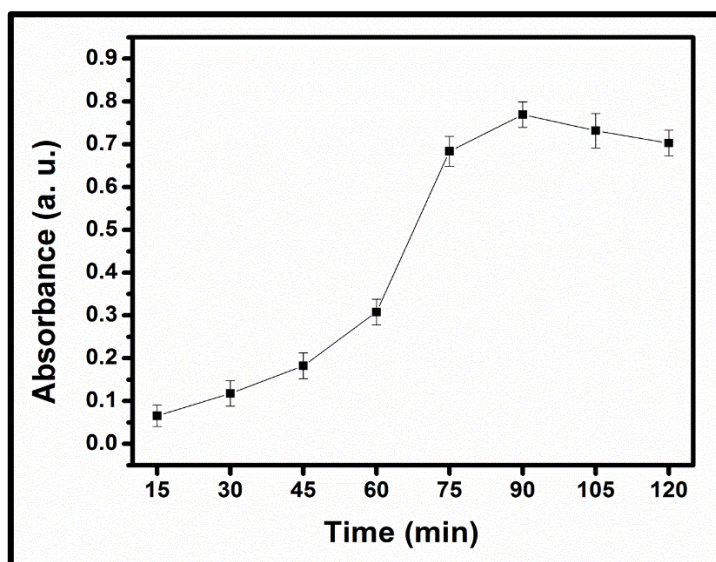
Fig. 3.4 Absorbance of a mixture of FeTe NRs (1.25 μg mL^{-1}) and Hg^{2+} ions (500 nM) against reaction time.

Figure 3.4 shows response curve against reaction time, showing that 90 min was optimal. The absorbance decreased slightly upon further increase in reaction time, mainly because of the decomposition of ABTS product. When the reaction was conducted at pH 4.0 and at the temperature range over 30–75 ºC for 90 min, the optimal temperature was 60 ºC (Fig. 3.5A).
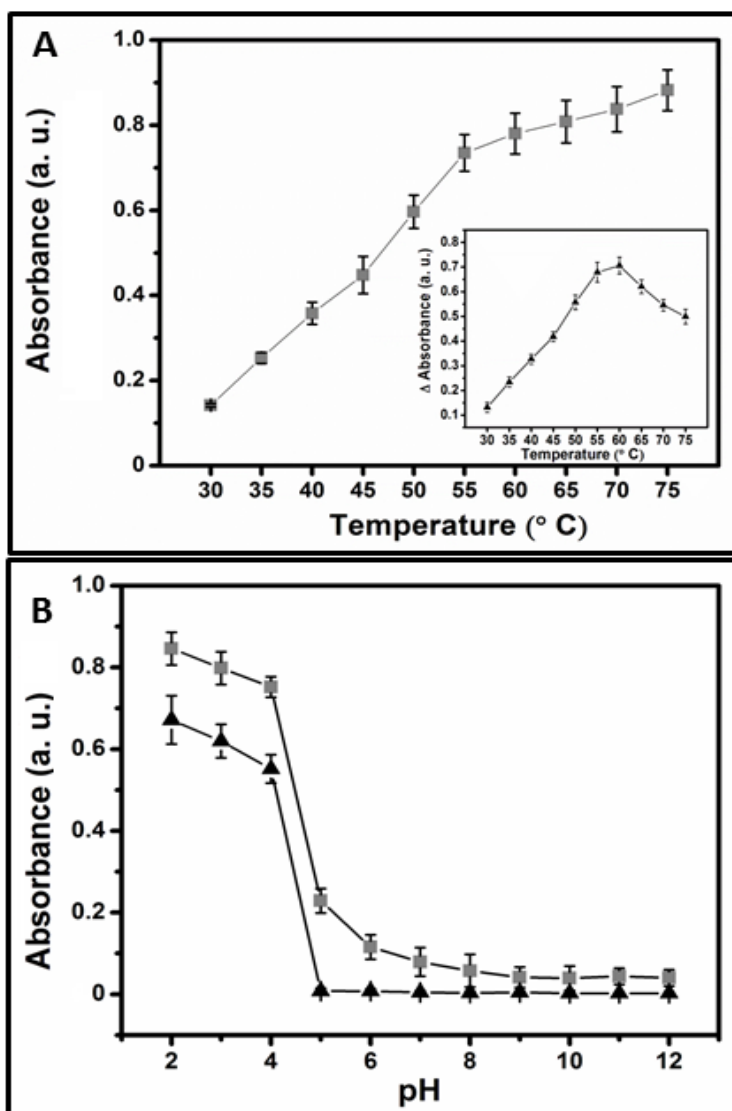
Fig. 3.5 (A) Temperature dependent response curves for the reaction between FeTe NRs and Hg^{2+} ions. Inset to (A) $\Delta A = A_{418}$ (in the presence of Hg^{2+} ions) $- A_{418}$ (in the absence of Hg^{2+} ions) against temperature. (B) pH dependent response curves (■ for FeTe NRs and ▲ for the control).

The kinetic energy increased upon increasing reaction temperature, accelerating the reaction. At a temperature higher than 60 ℃, the oxidation of Fe^{2+} by oxygen and decomposition of ABTS took place more rapidly. The solvent effect is negligible since our sensing mechanism is mainly through the reaction between FeTe

and Hg^{2+} ions, with support of no effect from methanol, ethanol, hexane and chloroform. We further investigated the pH effect on the reaction of the FeTe NRs with Hg^{2+} ions over pH values 2.0–12.0, as it might also play a critical role in the reaction of the FeTe NRs with Hg^{2+} ions. Taking the account of pH having a significant effect on the formation of iron oxide (at high pH values) and the dissolution of FeTe NRs (at low pH values).[27]

Figure 3.5B shows prominent differences in the absorbance values occurred at pH 3.0 and 4.0. At the pH values > 4.0, the formation of iron oxide and mercury hydroxide is a concern. The solubility product values of iron oxide and mercury hydroxide are 2.6×10^{-39} and 3.6×10^{-26}, respectively.[28] At the pH values < 3.0, dissolution of FeTe and HgTe NRs occurred.[29]

3.3.3 Detection of Hg^{2+} ions

Figure 3.6 shows that the absorbance of ABTS product increases upon increasing the Hg^{2+} concentration, displaying the dose response curve for the detection of Hg^{2+} ions, with a linear relationship between the absorbance and the $HgCl_2$ concentration ranging from 5 to 500 nM ($R^2 = 0.99$) and a linear range from 5 to 100 nM (Fig. 3.6A inset). This approach provided a limit of detection at a signal-to-noise ratio of 3 of 1.31 nM for Hg^{2+} ions.

We also conducted ICP-MS measurements to determine the amounts of the Fe and Hg in the as-formed HgTe NRs (100 nM). The amount of Fe^{2+} ions decreased upon increasing the amount of Hg^{2+} ion detected in the as-formed HgTe NRs (Fig. 3.7), further supporting the displacement of Fe^{2+} ions in the FeTe NRs by Hg^{2+} ions.
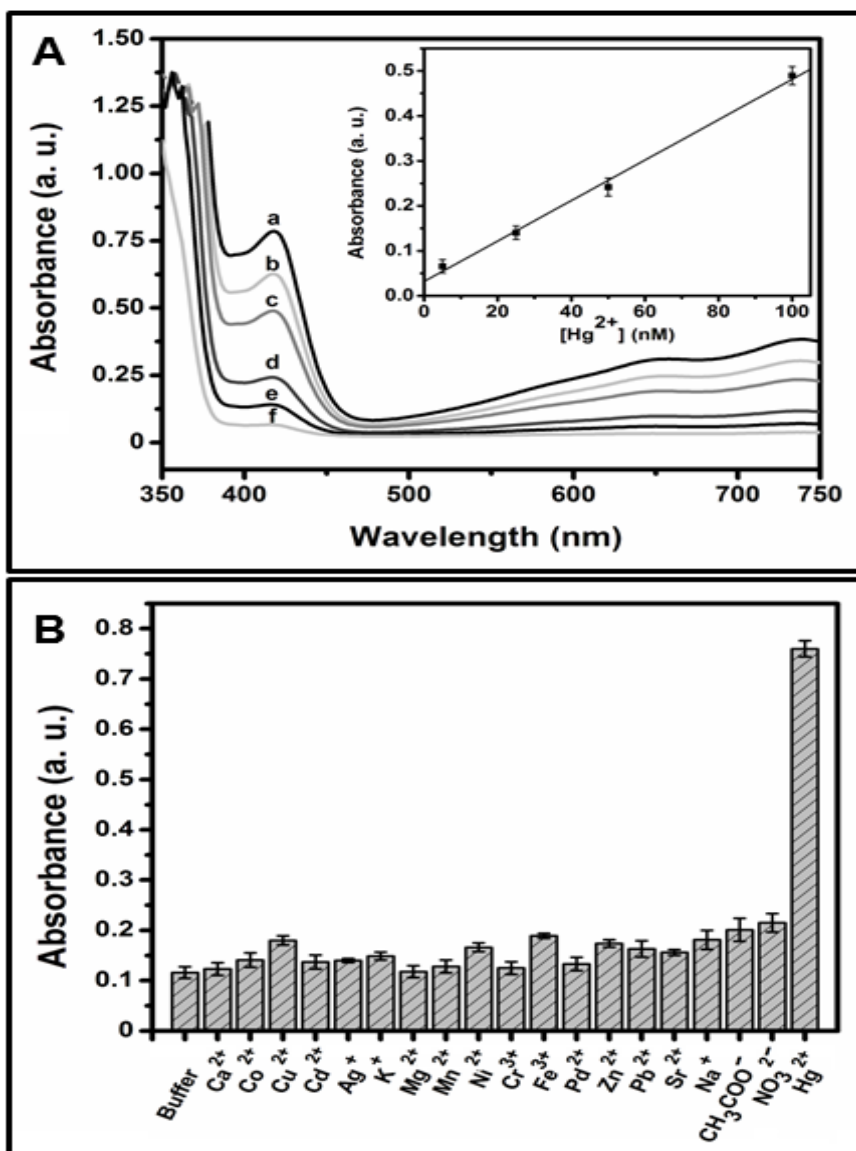
Fig. 3.6 (A) Absorption spectra of FeTe NRs solutions containing ABTS (60 mM) with H_2O_2 (0.1 μM) in the presence of Hg^{2+} ions at the concentrations of 5 to 500 nM (a: 5, b: 25, c: 50, d: 100, e: 250, f: 500 nM). Inset to (A): linearity of absorbance against Hg^{2+} concentration over a range of 5−100 nM.   (B) Selectivity of the assay using FeTe NRs for the detection of Hg^{2+} ions. Concentrations of metal ions are 50 nM for Hg(II) and 1 μM for the other metal ions.
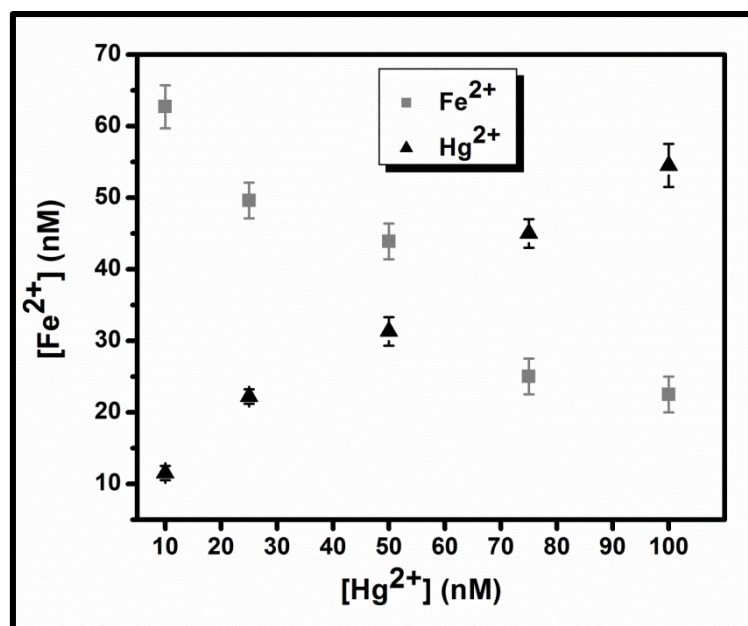
Fig. 3.7 The concentrations of Fe^{2+} ions remaining in the FeTe NRs against those for Hg^{2+} ions added. The concentrations of the two metal ions were determined by ICP-MS measurements. The reaction conditions are the same as in Fig. 2A. Hg^{2+} ions at the concentrations 10–100 nM were added to the FeTe NRs solution (0.32 µg mL^{-1}). After the reaction, the FeTe NRs were subjected to three cycles of centrifugation/wash and the pellets were dissolved in HNO$_3$ solution (5 mL, 2%).

3.3.4 Sensitivity and selectivity of FeTe NRs towards Hg^{2+} ions

Control experiments were carried out to test the specificity of the developed system for Hg^{2+} ions (50 nM) under optimal conditions in the presence of various metal ions and anions such as acetate and nitrate ions (each at a concentration of 1 µM). The results displayed in Fig. 3.6B reveal that the sensing system is specific to Hg^{2+} ions. Relative to the solubility product of HgTe (10^{-70}), those for the other metal complexes with Te^{2-} are much higher. In other words, the other metal ions relative to Hg^{2+} ions displaced Fe^{2+} ions from the FeTe NRs with much lower degree.[29, 30]

3.3.5 Analysis of real sample

To examine the practicality of our developed approach, the concentration of mercury in blood (SRM 955c) was determined. We determined the concentration of mercury in the spiked blood samples, with a linear plot ($R^2 = 0.99$) of the absorbance (Y) against the mercury concentration (X) as displayed in Fig. 3.8.
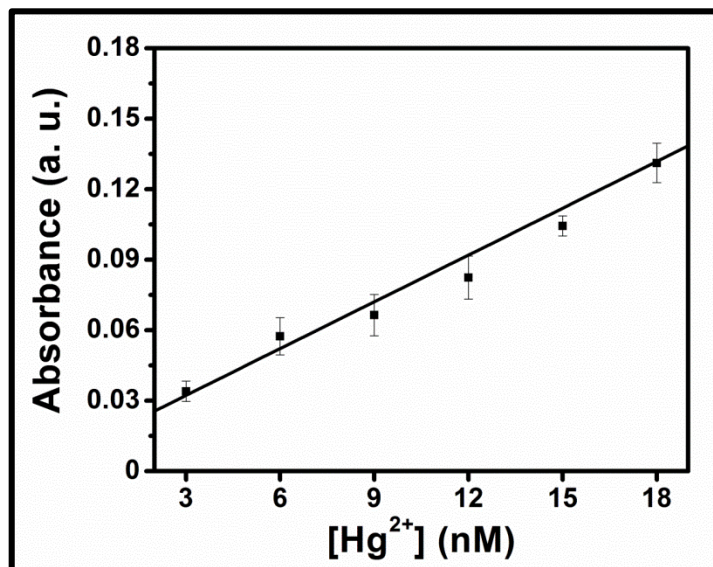
Fig. 3.8 Detection of Hg^{2+} ions using FeTe NRs in a representative spiked mercury blood sample (SRM 955c). The final concentrations of spiked standard Hg^{2+} ions are 3 to 18 nM. Five measurements were conducted for each sample.
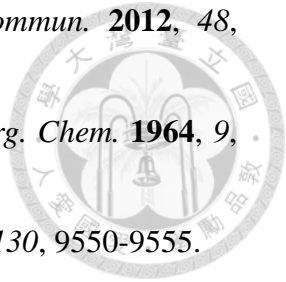
We calculated the mercury concentration using the above equation to be (8.70 $\pm$ 0.37) nM ($n = 5$). The certified concentration of mercury in the blood sample is (8.90 $\pm$ 0.80) nM. The t-value of 0.78 at a 95% confidence level was smaller than the t-value of 2.015 ($n = 5$), showing the two approaches provided results without significant difference. Our results reveal that our approach using FeTe NRs holds great potential for the determination of the concentration of mercury in biological samples.

3.4 Conclusions

We have developed a simple, sensitive, and selective sensing system using FeTe NRs for the detection of mercury through the release of Fe^{2+} ions that catalyzes the reaction of ABTS with H_2O_2. Because the solubility product of HgTe is relatively lower than those of other tested MTe (M = Ca^{2+}, Co^{2+}, Cu^{2+}, Cd^{2+}, Ag^+, K^+, Mg^{2+}, Mn^{2+}, Ni^{2+}, Cr^{3+}, Fe^{3+}, Pd^{2+}, Zn^{2+}, Pb^{2+}, Sr^{2+}, Na^+), the sensing approach is selective toward Hg^{2+} ions over other tested metal ions. The sensing approach was validated by the determination of the concentration of total Hg in a blood sample (SRM 955c), with a result showing no significant difference from the certified value. Relative to other optical approaches for detecting Hg^{2+} ions,[36] this approach provides comparable sensitivity, with an advantage of no need for masking agents.

References

(1) (No authors Listed), World Health Organ Tech Rep Ser. **1978,** *639,* 1-39.

(2) Zheng, W.; Aschner, M.; Ghersi-Egea, J.-F. *Appl. Pharm.* **2003**, *192,* 1-11.

(3) Nixon, D. E.; Mussmann, G.V.; Moyer, T. P. *J. Anal. Toxicol.* **1996**, *20,* 17-22.

(4) Hanna, C. P.; Tyson, J. F.; McIntosh, S. *Anal. Chem.* **1993**, *65,* 653-656.

(5) Leopold, K.; Foulkes, M.; Worsfold. P. *Anal. Chim. Acta.* **2010**, *663,* 127-138.

(6) Hanna, C.; McIntosh, S. *Atom. Spectrosc.* **1995**, *16,* 106-114.

(7) Parsons, P. J.; Barbosa, J. F. *Spectrochim. Acta Part B: Atom. Spectrosc.* **2007**, *62,* 992-1003.

(8) Pozebon, D.; Dressler, V. L.; Becker, J. S.; Matusch, A.; Zoriy, M.; Becker, J. S. *J. Anal. Atom. Spectrom.* **2008**, *23,* 1281-1284.

(9) Hasenacker, F.; Hirner, A.V. *J. Anal. Atom. Spectrom.* **2007**, *22,* 175-178.

(10) Cheng, X.; Li, Q.; Qin, J.; Li, Z. *ACS Appl. Mater. Interfaces.* **2010**, *2,* 1066-1072.

(11) Chen, K.-H.; Lu, C.-Y.; Cheng, H.-J.; Chen, S.-J.; Hu, C.-H.; Wu, A.-T.; *Carbohyd. Res.* **2010**, *345,* 2557-2561.

(12) Kim, S. K.; Swamy, K. M. K.; Chung, H. N.; Kim, M. J.; Jeong, Y.; Yoon, J. *Tetrahedron. Lett.* **2010**, *51,* 3286-3289.

(13) Soh, J. H.; Swamy, K. M. K.; Kim, S. K.; Kim, S.; Lee, S.-H.; Yoon, J. *Tetrahedron. Lett.* **2007**, *48,* 5966-5969.

(14) Zhang, J. F.; Lim, C. S.; Bhuniya, S.; Cho, B. R.; Kim, J. S. *Org. Lett.* **2011**, *13,* 1190-1193.

(15) Selid, P.; Xu, H.; Collins, E. M.; Collins, M. S. F.; Zhao, J. X. *Sensors.* **2009**, *9,* 5446-5459.

(16) Knecht, M. R.; Sethi, M. *Anal. Bioanal. Chem.* **2009**, *394,* 33-46.

(17) Lin, Y.-W.; Huang, C.-C.; Chang, H.-T. Analyst. **2011**, *136,* 863-871.

(18) Sumesh, E.; Bootharaju, M. S.; Anshup. T; Pradeep, T. *J Hazard Mater.* **2011**, *189,* 450-457.

(19) Campos, B. B.; Algarra, M.; Alonso, B.; Casado, C. M.; Esteves da Silva, J. C. G. *Analyst.* **2009**, *134,* 2447-2452.

(20) Lin, Z.-H.; Yang, Z.; Chang, H.-T. *Cryst. Growth Des.* **2007**, *8,* 351-357.

(21) Roy, P.; Lin, Z.-H.; Liang, C.-T.; Chang, H.-T. *Chem. Commun.* **2012**, *48*, 4079-4081.

(22) Buketov, E. A.; Ugorets, M. Z.; Pashinkin, A. S, *Russ. J. Inorg. Chem.* **1964**, *9*, 292-294.

(23) Wark, S. E.; Hsia, C. H.; Son, D. H.; *J. Am. Chem. Soc.* **2008**, *130*, 9550-9555.

(24) Mizera, E.; Klimkiewicz, M.; Pajązkowska, A.; Godwod, K.; *Phys. Status Solidi.* **1980**, *58*, 361-366.

(25) Globus, A.; Pascard, H.; Cagan, V. *J. De. Phys. Coll.* **1977**, *38*,163-168.

(26) Xia, T. L.; Hou, D.; Zhao, S. C.; Zhang, A. M.; Chen, G. F.; Luo, J. L.; Wang, N. L.; Wei, J. H.; Lu, Z. Y.; Zhang, Q. M. *Phys. Rev. B*. **2009**, *79*, 140510-1-140510-4.

(27) Banfalvi, G. *Chemosphere*. **2006**, *63*, 1231-1234.

(28) Meighan, M.; MacNeil, J.; Falconer, R.; *J. Chem. Educ.* **2008**, *85*, 254-255.

(29) Moon, G.; Ko, S.; Xia, Y.; Jeong, U. *ACS Nano*. **2010**, *4*, 2307-2326.

(30) Garadkar, K.; Pawar, S.; Hankare, P.; Patil, A. *J. Alloy. Compd.* **2010**, *491*, 77-80.

Chapter 4

Synthesis of Graphene-ZnO-Au Nanocomposites for Efficient Photocatalytic Reduction of Nitrobenzene

4.1 Introduction
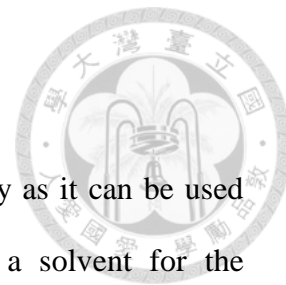
Nitrobenzene (NB) is an attractive chemical in the industry as it can be used for the manufacture of aniline, soaps, metal polishes, and as a solvent for the preparation of cellulose ester from cellulose acetate.[1] It is however carcinogenic and genotoxic to human beings, causing diseases such as methaemoglobinaemia.[1] A permissible limit of 17 ppm (13.8 μM) for NB in lakes and streams has been set by the U.S. Environmental Protection Agency (EPA). The exposure limit of NB to human beings is 5 mg m^{-3} for an 8h-work day.[1] NB has a high Hammet constant (0.71) and is one of the most difficult aromatic compounds to be oxidized.[2] This has prompted many researchers to focus on the reduction of NB using microbial, chemical, and catalytic methods.[3-9] Anaerobic reduction with microbial cultures often takes an extremely long time extending to more than a week. In addition, it is difficult to handle high concentrations of NB. Chemical reduction using inexpensive iron (0) is a common technique, however inactive ferric oxide forming on its surface due to corrosion is problematic.[10] In addition, its use is limited to neutral conditions. Catalytic hydrogenation is efficient in the treatment of wastewater, but it is expensive. Alternatively, electrochemical techniques are efficient in the reduction of NB, but the production of hazardous byproducts (e.g. phenylhydroxylamine and nitrophenol) is a concern.[7]

Nanoparticles (NPs) such as TiO_2,[4, 11] ZnO[12] and CdS[13] having great surface areas and high surface energies have emerged as useful photocatalysts for the degradation of various hazardous compounds such as NB and phenol.[4, 11, 13] Surface modification of photocatalysts such as TiO_2 with amino acids or organic acids has been found effective to provide better electron transfer between TiO_2 NPs and NB,

leading to greater photoreduction[14,15] of NB.

Semiconductor NPs, however provide high activity by generating electron-hole pairs only under UV light irradiation. In order to improve their efficiency in the visible region, surface modification of the photocatalysts with metal or metal oxides such as B-Ni, Fe^{3+}, and VO_3^- has also been demonstrated.[16,17, 18] However, transition metal doping commonly suffers from the formation of a discrete level in the forbidden band of the photocatalyst, resulting in low-mobility of electrons and holes in the dopant level and thus limiting their activity enhancement.[19] Recently, NPs decorated onto the surface of graphene have become interesting catalysts for the degradation of various compounds and production of hydrogen by taking advantage of strong absorption in the UV region, high electrical conductivity, and large surface area of graphene.[20-25] In addition, a wide band gap, the presence of large number of surface states, and availability of valence and conduction band edges from metal NPs such as Au can be obtained. With the synergetic effect and efficient electron transfer, graphene-ZnO and graphene-Au have been shown as efficient photocatalysts for the degradation of nitroaromatic compounds.[26,27] When using semiconductor photocatalysts, excitation of electrons is accomplished by the absorption of photons with energy equal to or higher than their bandgaps. This light-induced generation of electron-hole pairs is a prerequisite step in all semiconductor mediated photocatalytic processes. Although ZnO is an efficient photocatalyst for the reduction of various pollutants,[28-31] recombination of the electron-hole pair due to low kinetic barrier during the reactions is a major problem, leading to poor quantum efficiency. In order to circumvent this problem, graphene oxide (GO), zinc acetate, catechin, and Au nanorods (NRs) in the presence of ethylenediamine (EDA) were used to prepare G-ZnO-Au nanocomposites (NCs). The NCs provided great photocatalytic activity,
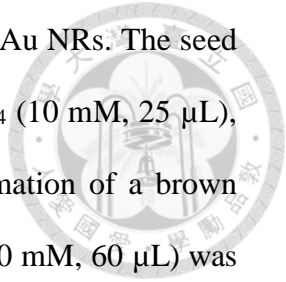
mainly because of efficient electron transfer provided by graphene, strong UV absorption provided by the ZnO nanospheres (NSs), and efficient charge separation from Au NRs.[3] The roles played by graphene, ZnO NSs, and Au NRs[32] in determining their photocatalytic activity for the reduction of NB were explored separately by controlling their amounts. The G-ZnO-Au NC allowed rapid reduction of NB under UV light irradiation. To detect the product and the intermediates, as well as to understand their extremely high photocatalytic activity toward NB, surface assisted laser desorption/ionization mass spectrometry (SALDI-MS) and electrochemistry were conducted. Our results reveal that the cost-effective G-ZnO-Au NC is efficient for the reduction of NB, showing its potential as a catalyst for removal of NB or for the production of aniline from NB.

4.2 Experimental Section

4.2.1 Materials

Ascorbic acid, hexadecyltrimethylammonium bromide (CTAB, 99%), sodium borohydride (98%), and zinc acetate (99%) were purchased from Acros (Geel, Belgium). Catechin hydrate (98%), EDA (99.5%), hydrogen tetrachloroaurate (HAuCl$_4$), NB (99%), titanium dioxide NPs (P25), and silver nitrate (AgNO$_3$, 99%) were purchased from Sigma Aldrich (St. Louis, MO, USA). Methanol (99.5%), ethanol (99.5%), and isopropanol (99.5%) were purchased from Shimakyu's Pure Chemicals (Osaka, Japan). GO was bought from Graphene Supermarket (Calverton, NY, U.S.A). Ultrapure water was obtained using a Milli-Q ultrapure (18.2 MΩ cm^{-1}) system.

4.2.2 Synthesis of Au NRs

A seed mediated method was applied for the preparation of Au NRs. The seed solution was prepared by mixing ultrapure water (475 µL), $HAuCl_4$ (10 mM, 25 µL), and CTAB (0.2 M, 500 µL) in a glass bottle, leading to the formation of a brown solution. Subsequently freshly prepared ice cold aqueous $NaBH_4$ (10 mM, 60 µL) was injected into the solution and the mixture was vigorously stirred, which was then diluted 10 times with ultrapure water. This seed solution was kept at ambient temperature (25 ℃) for 10 min before use. The growth solution was prepared by mixing ultrapure water (5 mL), $HAuCl_4$ (10 mM, 1 mL), and CTAB (0.2 M, 10 mL) in a glass bottle (20 mL) to form a brown solution. $AgNO_3$ (4 mM, 0.2 mL) was immediately added to the solution, followed by the addition of ascorbic acid (7.88 mM, 1.4 mL), leading to the formation of a colorless solution. Upon adding $AgNO_3$ into aqueous CTAB solution, AgBr was formed on the surfaces of Au nanoparticles to restrict their growth.[33] The underpotential deposition of metallic silver on the different crystal facets of gold also leads to symmetry breaking, leading to the formation of Au NRs with a high aspect ratio. The resultant solution was gently stirred, followed by addition of the seed solution (2.4 mL). The mixture was kept under constant stirring for about 1 h as the color changed to dark red. The obtained Au NRs were subsequently centrifuged at relative centrifugation force (RCF) of 12,000 *g* for 10 min and washed twice with ultrapure water (2 x 10 mL) prior to use.

4.2.3 Synthesis of G-ZnO-Au NCs

Ultrapure water (4 mL), zinc acetate (0.1575 g), and EDA (0.13 M, 1 mL) were added sequentially into a glass bottle (10 mL). The solution was then stirred for 5 min at 90 ℃. Catechin (20 mg) was next added to the solution, leading to a color change from colorless to orange. To the orange solution, GO solution (5 mg mL^{-1}, 0.5
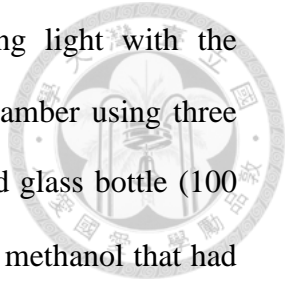
mL) and the as-prepared Au NRs (0.25 mL) that had been stirred for 10 min were mixed, which were then stirred vigorously for 1 h, leading to a color change from orange to dark brown. This solution was then reacted in an autoclave at a temperature of 300 ℃ for 2 h. The obtained G-ZnO-Au NCs were subsequently centrifuged at RCF 25,000 g for 10 min and washed twice with ultrapure water (2 x 10 mL) prior to use.

4.2.4 Characterization of G-ZnO-Au NCs

A double-beam UV–vis spectrophotometer (Cintra 10e, GBC) was used to record the absorption spectra of the Au NRs and G-ZnO-Au NCs. JEOL JSM-1230 and FEI Tecnai-G2-F20 TEMs were used to measure the sizes and shapes of the as-prepared G-ZnO-Au NCs. The re-dispersed G-ZnO-Au NCs were separately placed on formvar/carbon film Cu grids (200 mesh; Agar Scientific) and dried at ambient temperature. XRD patterns of the NCs were measured using a PANalytical X'Pert PRO diffractometer (PANalytical B.V., EA Almelo, Netherlands) and Cu-Ka radiation (λ = 0.15418 nm); the samples were prepared on Si substrates. An energy dispersive X-ray (EDAX) system (Inca Energy 200, Oxford) was used to determine the composition of the as-prepared NCs. Raman spectra were recorded using a Raman spectrometer (Dong Woo 500i, Korea) equipped with a 50× objective and a charge-coupled detector. The excitation wavelength was 532 nm and the spectral aperture was 50 µm. The signal collection time for each sample was 30 s.

4.2.5 Photocatalytic Reduction of Nitrobenzene

Experiments were carried out in an apparatus specially designed for the photocatalytic reaction. A 500-W UV-vis lamp (Newport, Oriel Instrumentation,

Irvine, California, USA) with a cut off filter used for blocking light with the wavelength above 420 nm was placed in a well-aerated empty chamber using three fans to maintain the reactor temperature at 30 $^\circ$C. A wide mouthed glass bottle (100 mL) contained NB (5 mM, 50 mL) and G-ZnO-Au (4 mg mL^{-1}) in methanol that had been subjected to sonication for 10 min. The reaction solutions prior to and during the course of the reaction were purged with N_2 in order to remove any dissolved oxygen. The pH value of the reaction solution was 10.0. The distance between the light source and the mouth of the glass bottle was 8 cm. The reaction solution was kept under illumination for 140 min. At certain intervals of time, aliquots (1 mL) of the solution were taken out. After being centrifuged at 10000g for 10 min to remove the particles, the absorbance of each supernatant at λ_{max} = 276 nm was recorded. The concentrations of NB in the solution at various reaction times were determined (n = 5) using a calibration curve of absorbance against standard NB solutions (0.01–10 mM).

4.2.6 Electrochemical Reduction of Nitrobenzene

The G-ZnO-Au NCs (4 mg mL^{-1}) were loaded onto a clean FTO electrode. The FTO electrode was then placed in an oven at 60 ºC to calcine the G-ZnO-Au NCs. Cyclic voltammetry measurements were carried out using a CHI 760 electrochemical workstation (CH Instruments, USA) with a three-electrode system consisting of a working electrode (G-ZnO-Au NC modified FTO electrode), a platinum wire counter electrode (0.5 mm diameter), and an Ag/AgCl (saturated KCl) reference electrode. A phosphate buffer solution (0.1 M, 25 mL, pH 7.0) containing 10 mM KCl and NB (5 mM) was stirred and purged with nitrogen gas before and during electrolysis. The experiments were carried out at ambient temperature.

4.2.7 SALDI-MS

SALDI-MS was used to determine the products and intermediates formed upon the reduction of NB using the G-ZnO-Au photocatalyst. Aliquots (1.0 µL) of mixtures were pipetted onto a stainless-steel 96 well MALDI target (Bruker Daltronics) and dried in air at ambient temperature for 1 h prior to SALDI-MS measurements. SALDI-MS was conducted in a positive-ion mode on a reflectron-type time-of-flight (TOF) mass spectrometer (Biflex III, Bruker) equipped with a 1.25-m flight tube. The samples were irradiated with a nitrogen laser (emission at 337 nm) at 10 Hz (pulse duration 4 ns). Ions produced by laser desorption were stabilized energetically during a delayed extraction period of 200 ns and then accelerated through a linear TOF reflection before entering the mass analyzer. The accelerating voltage was set at 20 kV. To obtain good resolution and signal-to-noise (S/N) ratios, the laser fluence was adjusted to slightly higher than the threshold and each mass spectrum was generated by averaging 300 laser pulses.

4.2.8 Reusability

The G-ZnO-Au NCs were subjected to multiple cycles (n = 5) of photocatalytic degradation of NB. After completion of each cycle (140 min), we collected the photocatalyst through centrifugation at RCF 25,000 g for 20 min, followed by washing thoroughly with ultrapure water. The procedure was repeated for the second to fifth consecutive cycles.

4.3 Results and Discussion

4.3.1 Physical and Chemical Properties of G-ZnO-Au NCs

Fig. 4.1A shows the TEM image of the G-ZnO-Au NCs consisting of graphene

sheets, ZnO NSs (45.3 ± 3.7) nm; 100 counts), and Au NRs (the length and width were (26.2 ± 1.5) and (14.1 ± 1.3) nm, respectively). The X-ray diffraction (XRD) pattern of the G-ZnO-Au NCs (Fig. 4.1B) shows the major peaks corresponding to graphitic carbon (JCPDS No. 75-1621) at 24.9° (0 0 2), hexagonal ZnO (JCPDS No. 36-1451) at 31.5° (1 0 0), 34.35° (0 0 2), 36.13° (1 0 1), 47.40° (1 0 2), 56.33° (1 1 0), 66.35° (2 0 0), 67.60° (1 1 2), and 68.85° (2 0 1), and Au (JCPDS No. 04-0784) at 63.98° (2 2 0).[27, 28] The Raman spectrum of G-ZnO-Au NCs is displayed in Fig. 4.1C, showing two bands at 1340 and 1590 cm^{-1} that correspond to the disordered (D) band and graphitic (G) band of carbon materials, respectively. The peak at 440 cm^{-1} corresponds to E2 (high) mode and that at 582 cm^{-1} is assigned to E1 (longitudinal optical, LO) mode associated with the structural defects in ZnO.[29] The band at 1200 cm^{-1} is due to the CTAB that was capped onto the Au NRs.
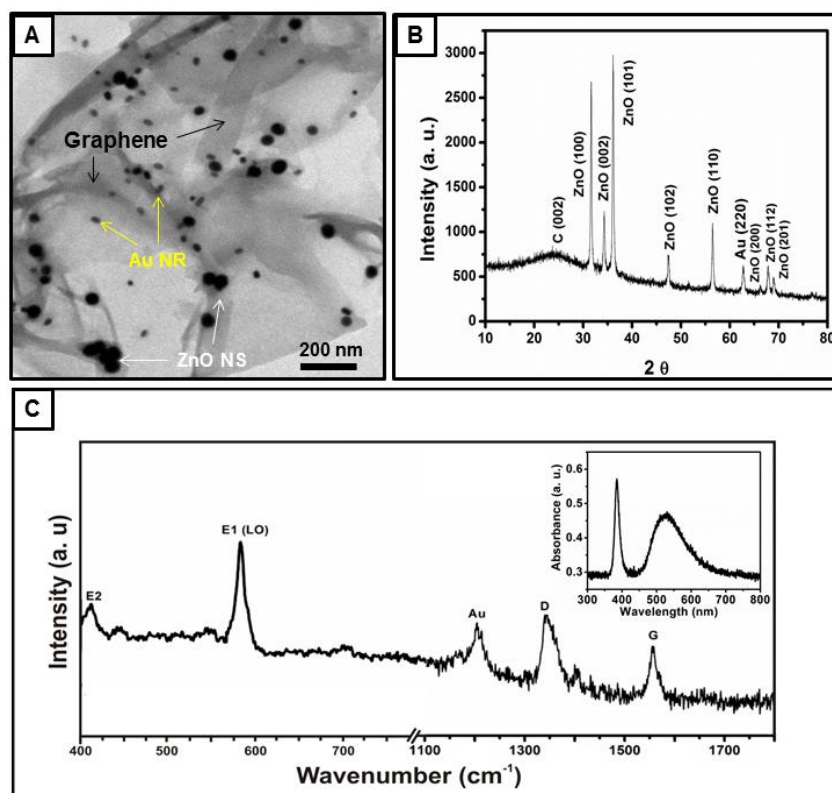
Fig. 4.1 (A) TEM image, (B) EDAX spectrum, and (C) Raman spectrum of G-ZnO-Au NCs, Inset to C: UV-Vis absorption spectrum of ZnO NS's.

The UV-vis spectrum of ZnO NSs (Inset to Fig. 4.1C) shows two characteristic absorption peaks at 390 and 510 nm,[37] respectively revealing their large excitonic binding energy. The absorption peak at 510 nm is due to the absorption by the trap centers present on the surface of the ZnO NSs that are produced due to oxygen vacancy related surface defects when synthesized at high temperatures (< 300 ºC).[38, 39] The energy dispersive X-ray (EDAX) pattern in Fig. 4.2A displays intense peaks for the elements Zn and O, which confirms the formation of ZnO NSs.[31] Although two absorption peaks centered at 526 and 712 nm are apparent in the free Au NRs (Fig. 4.2B Inset), they are almost negligible in the G-ZnO-Au NCs, mainly because of their small amount that is supported by an Au peak in Fig. 4.1B. The corresponding EDAX pattern of Au NRs (Fig. 4.2B) reveals existence of a pure gold phase.[32]
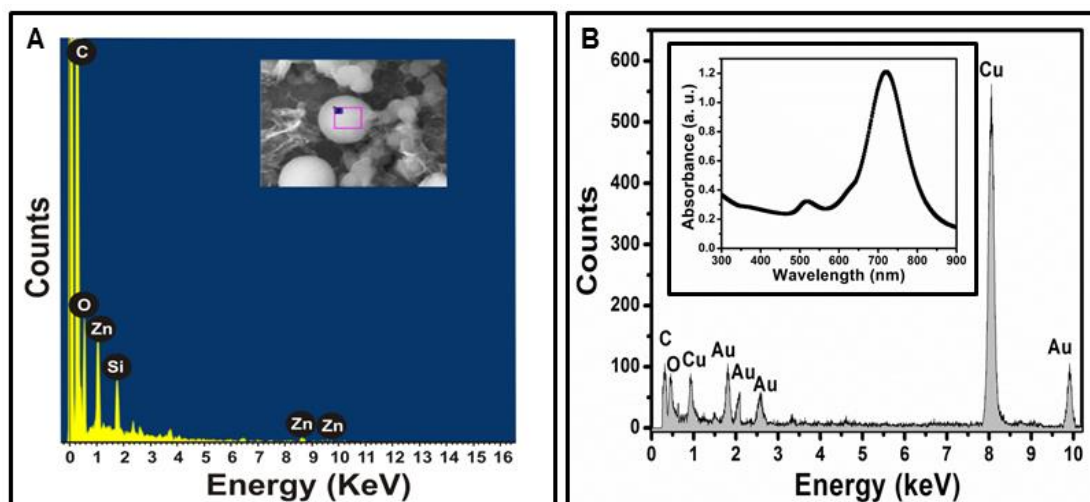
Fig. 4.2 EDAX spectrum of **(A)** ZnO NS and **(B)** Au NR in G-ZnO-Au NC. Insets: (A) SEM image of the ZnO NS and (B) Absorption spectrum of Au NRs.

4.3.2 Photocatalytic Reduction of Nitrobenzene

The degradation of NB was conducted to evaluate the photocatalytic activity of the prepared G-ZnO-Au NCs. Fig. 4.3A shows various effects of three solvents on

the photocatalytic reduction of NB, revealing that methanol is superior to ethanol and isopropanol. The reductions were completed within 140, 160, and 330 min, when using methanol, ethanol, and isopropanol, respectively, the photo-catalytic reduction was initiated by the photo-generated holes (h^+) and electrons (e^-) when the G-ZnO-Au NC was illuminated under UV light. The hydroxyl groups (OH) in methanol inhibited the h^+/e^- recombination by scavenging and trapping the photo-generated holes, leading to producing hydroxyl radicals (OH$^.$) that enabled the photo-excited electrons to reduce NB to aniline.[33]

A primary alcohol as a solvent has a higher yield in comparison to a secondary alcohol, which affects the electron transfer kinetics.[33] Methanol acts as a hole scavenger to inhibit the recombination of the photo excited electron-hole pair, mainly because of its capability for capturing photo-excited holes. In addition, its lower viscosity, higher polarity, and lower polarizability are taken into account. We also studied the effect of dissolved oxygen on the reduction of NB by purging with N_2 prior to and during the course of the reaction.

Fig. 4.3B shows that the reduction conversion of NB to aniline is more efficient when there is no oxygen during the photocatalytic reduction process. The presence of oxygen is undesirable during the photocatalytic reduction as it tends to compete for the photo-generated electrons.[33] Fig. 4.4A shows that the maximum reduction of NB occurred between 0 to 60 min.
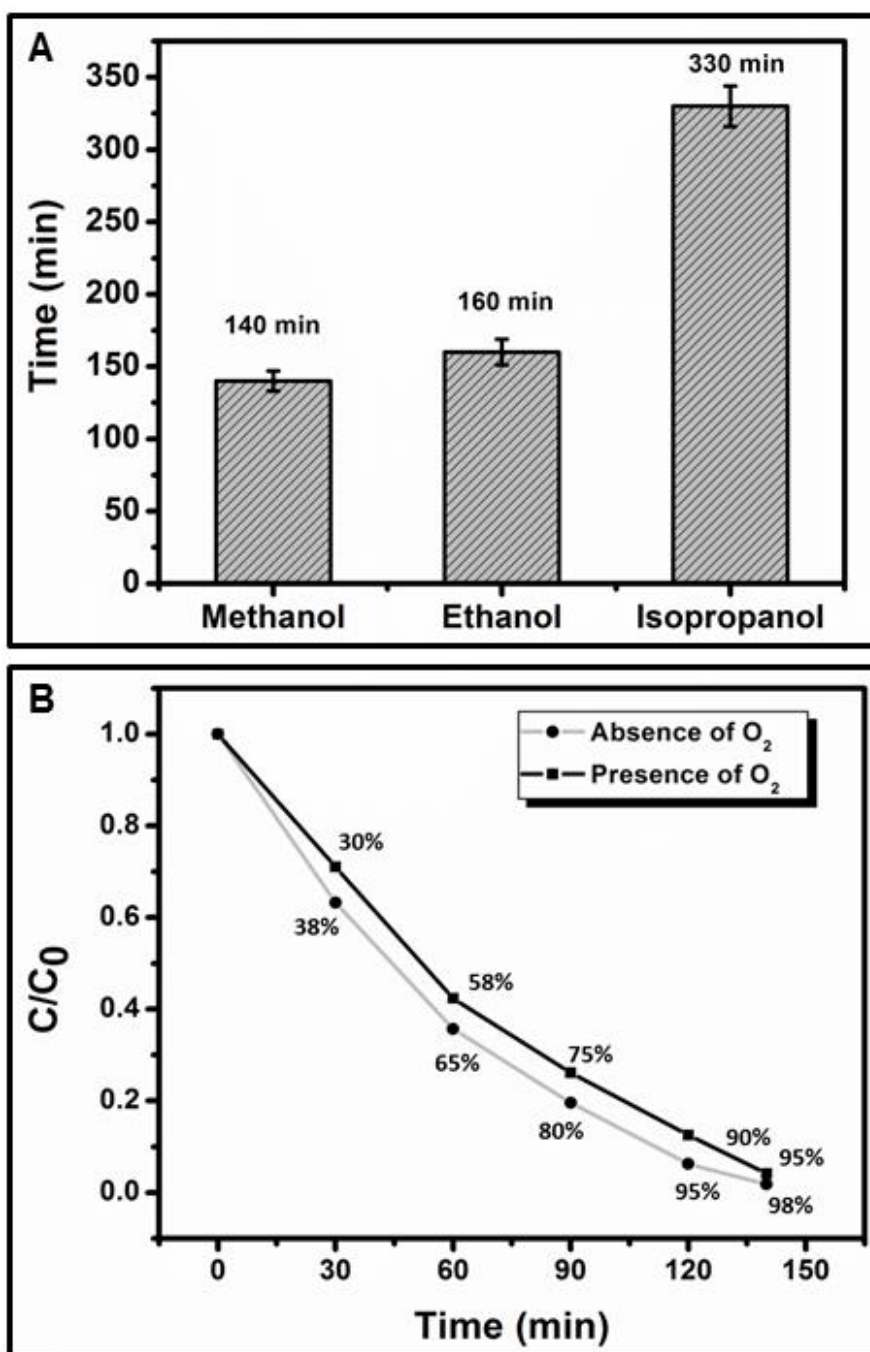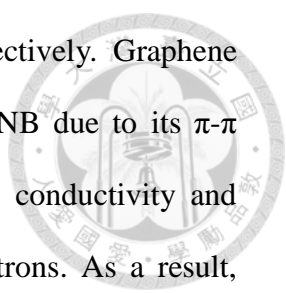
Fig. 4.3 Effects of **(A)** solvent and **(B)** oxygen on the photocatalytic reduction of nitrobenzene to aniline.
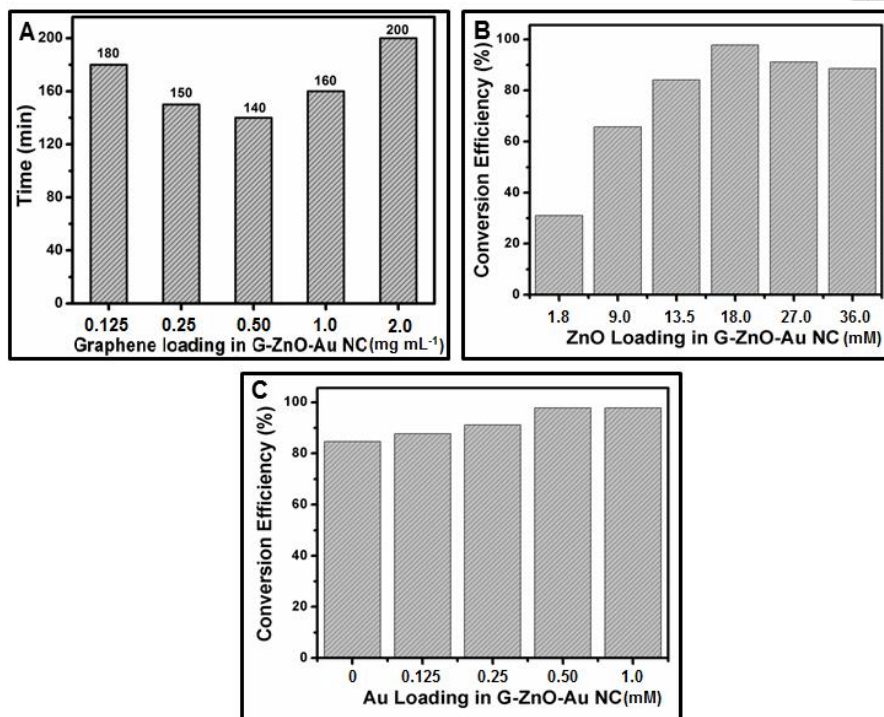
Fig. 4.4 Effect of (A) amount of graphene, (B) ZnO NS, and (C) Au NRs on the photocatalytic reduction of nitrobenzene to aniline. (A) Concentrations of ZnO NS and Au NRs are 18 mM and 0.5 mM, respectively. (B) Concentrations of graphene and Au NRs are 0.5 mg mL^{-1} and 0.5 mM, respectively. (C) Concentrations of graphene and ZnO NS are 0.5 mg mL^{-1} and 18 mM, respectively.

Figure 4.5B shows the degradation *(C/C$_0$)* of NB in the absence of various photocatalytic components and in the presence of one of the following photocatalysts: graphene, Au NRs, ZnO NS, commercial P25, G-Au NRs, G-ZnO NS, and G-ZnO-Au NCs. It can be seen that in the absence of a photocatalyst (curve a) and in the presence of graphene (curve b) reduction of NB was negligible. Au NRs (curve c) and ZnO NS (curve d) did catalyze the reduction of NB, with degradation rates 7- and 4.5-fold lower than that of the G-ZnO-Au NCs. Commercial P25 (curve e), G-Au NRs (curve f), and G-ZnO NSs (curve g) all catalyzed the reduction of NB, with degradation rates

3.5-, 3-, and 1.5-fold lower than that of G-ZnO-Au NCs, respectively. Graphene played a critical role in the efficient photocatalytic reduction of NB due to its π-π interaction with NB and great surface area.[34] Its great electrical conductivity and highly efficient charge transfer led to more photo-generated electrons. As a result, these photo-generated electrons from G-ZnO-Au NCs moved easily from within the inner confines of the photocatalyst to the surface, which resulted in efficient photocatalytic reduction of NB. The effect of graphene content was also investigated showing that its concentration at 0.5 mg mL^{-1} was optimal (Fig. 4.4A). When the concentrations of graphene were lower than 0.5 mg mL^{-1}, the photocatalytic activity of the G-ZnO-Au NCs was lower; longer reduction times of 150 and 180 min were required at the graphene concentrations of 0.25 and 0.125 mg mL^{-1}, respectively. On the other hand, the decrease in the photocatalytic performance at the graphene concentration greater than 0.5 mg mL^{-1} is mainly attributed to lower density of ZnO and Au NRs on the graphene surfaces, leading to lower efficiency in absorbing light. There is also a possibility that too much graphene could act as a recombination center instead of inhibiting the electron hole pair formation.[25, 35, 36] Fig. 4.5B shows the effect of ZnO loading on the conversion efficiency for the degradation of NB (5 mM), showing increases upon increasing the ZnO loading up to 18 mM, mainly because of increased number of active sites for adsorption and larger number of electron hole generation. When ZnO loading was further increased to 36 mM, increases in the opacity of the solution due to the aggregation of the particles occurred, leading to decreases in the photon flux penetration and thus decreases in the conversion efficiency. The optimal concentration of ZnO loading was found to be 18 mM. Au NRs assisted in maintaining efficient charge separation due to the presence of a surface charge barrier between ZnO and Au, thereby reducing the odds of h$^+$/e$^-$

66

recombination in ZnO.[37] Upon increasing the amounts of Au NRs (0.125, 0.25, and 0.5 mM) in the G-ZnO-Au NCs (Fig. 4.5C), the photocatalytic reduction efficiency of NB to aniline increased.
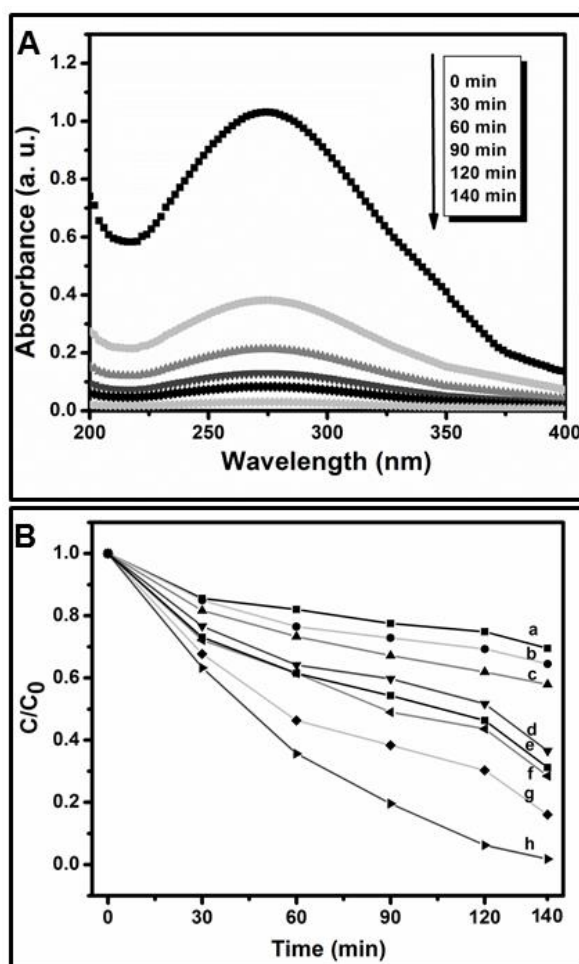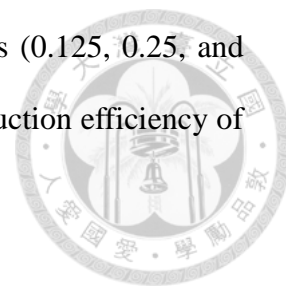
Fig. 4.5 (A) UV-vis absorption spectra of nitrobenzene after photoreduction or various times using G-ZnO-Au NCs. (B) Reduction rate of nitrobenzene in the (a) absence of any photocatalyst, and in the presence of (b) graphene (c) Au NR (d) ZnO NS (e) P25 (f) G-Au NR (g) G-ZnO NS, and (h) G-ZnO-Au NC. *C_0 and C* are the initial concentration of nitrobenzene and that at reaction times t, respectively.

The reduction efficiencies were 86%, 91%, and 97.8% in the presence of 0.125, 0.25, and 0.5 mM Au NRs, respectively. There was only a slight increase in the reduction

efficiency when Au NRs was increased from 0.5 to 1 mM. The G-ZnO-Au NCs possess greater photocatalytic activity toward the reduction of NB when compared to other photocatalysts (Table 1),[4-8]
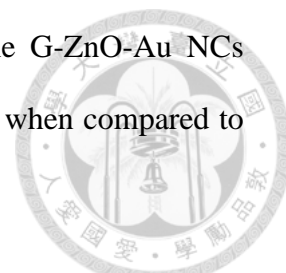
Method	Photocatalyst	Degradation Time (h)	Products	Yield	Reference
Photocatalytic Reduction	TiO_2	6	Aniline (Major) Nitrosobenzene and N-hydroxylaniline (By Products)	88.5%	4
Photocatalytic Reduction	TiO_2	24	Aniline (Major) Phenylhydroxylamine and Nitrosobenzne (Intermediates)	N/A	6
Chemical Reduction	Fe^0	72	Aniline (Major) Iron Oxide (By Products)	N/A	10
Electrochemical Reduction	Fe^{2+}, Cu^{2+} on an oxygen diffused electrode	7	ortho, meta and para-Nitrophenol	95%	46
Anaerobic degradation	Microorganisms	< 2 weeks	Various nitroaromatic compounds	95%	9
Photocatalytic Reduction	G-ZnO-Au NC	2h 20 min	Aniline Nitrosobenzene (By Products)	97.8%	Our Work

Table 4.1 Photocatalytic performance of G-ZnO-Au NCs for the reduction of nitrobenzene in comparison to other photocatalysts.

This is largely because of their facilitation of inter electron transfer and electronic interaction as intimate contact between ZnO and graphene was established. In addition to having lower catalytic activity relative to the G-ZnO-Au NC, TiO_2 has a high oxidation potential (2.7 V) and exhibits poor selectivity.[37] Based on the data obtained above, the mechanism of photocatalytic activity of the G-ZnO-Au NC

toward the reduction of NB was proposed as displayed in Scheme 4.1.
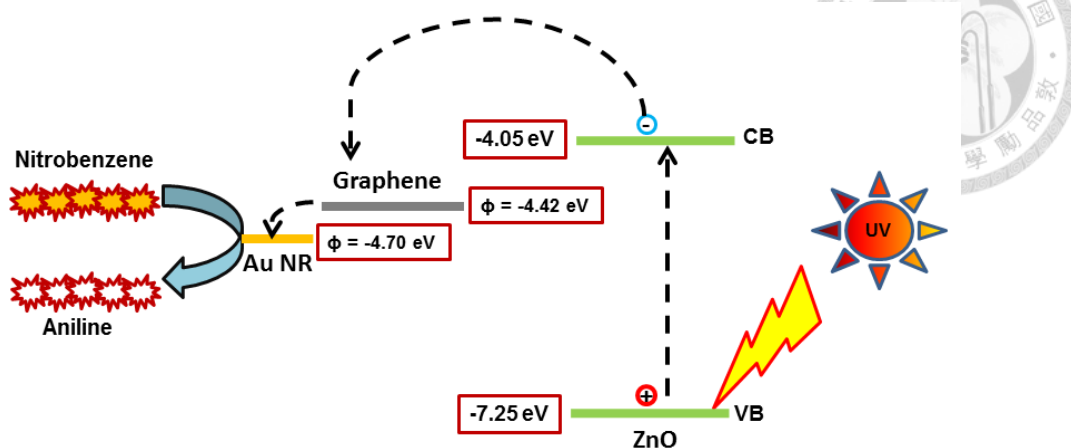
Scheme 4.1 Schematic diagram showing a plausible mechanism involved in the transfer of electrons from different energy levels of the G-ZnO-Au NCs for the photo-degradation of NB. CB and VB correspond to the conduction and valence band edges of ZnO. The symbol Φ corresponds to the work function of graphene and Au.

Under irradiation with UV light, a large number of free electrons in the conduction band and holes in the valence band are generated. The valence and conduction bands of ZnO have work functions of -7.25 eV and -4.05 eV (vs. vacuum), respectively.[12] On the other hand, the work functions of graphene and Au NRs are -4.42 eV and -4.70 eV, respectively.[12, 38, 39] As a result, the electrons transferred rapidly from ZnO to graphene, minimizing h^+/e^- recombination and thus leading to rapid reduction of NB within the first 60 min. The reusability of the photocatalyst was also investigated as displayed in Fig. 4.6 The catalytic degradation rates of the G-ZnO-Au NCs for NB after 5 cycles kept almost constant (less than 5% decrease in the conversion efficiency), showing great durability. Slight decreases in the rates were mainly due to loss of the G-ZnO-Au NCs through centrifugation/wash processes. The results revealed that the low-cost, efficient, and durable G-ZnO-Au NCs hold great potential for the reduction of NB. Instead of using more expensive metal-based

catalysts such as palladium and ruthenium,[40, 41] the G-ZnO-Au NCs might be a suitable candidate for the large-scale production of aniline from NB.
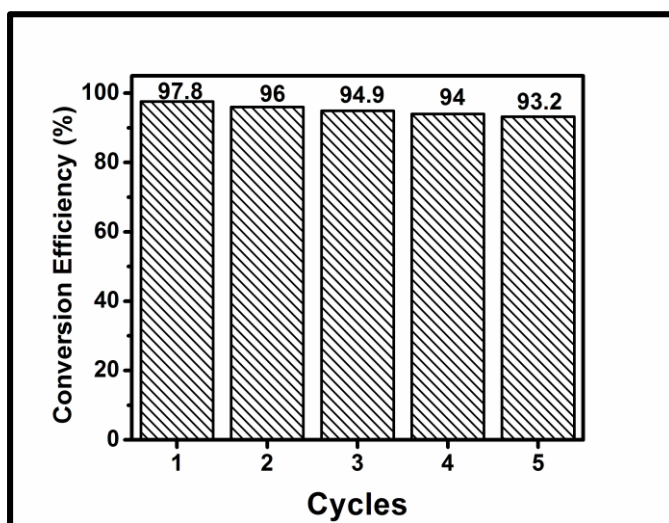
Fig. 4.6 Conversion efficiencies of nitrobenzene to aniline using G-ZnO-Au NC for the first five cycles.

The G-ZnO-Au NC also has an additional advantage of not producing any major toxic by-products.
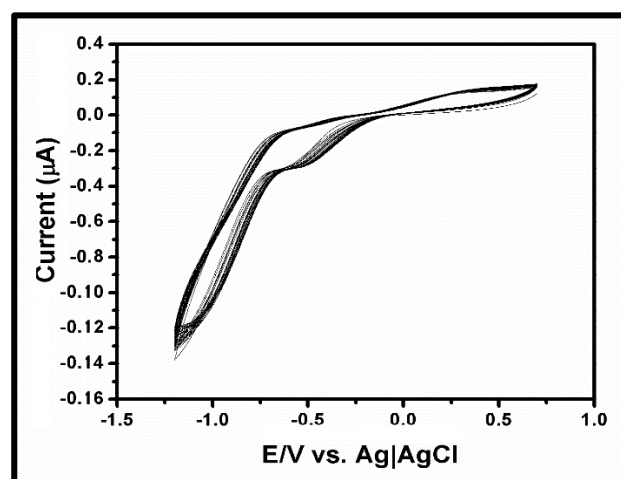
Fig. 4.7. Consecutive cyclic voltammograms (30 cycles in 30 min; 1 min/each cycle) recorded at the G-ZnO-Au NC modified FTO electrode.

The Fig. 4.7 shows consecutive cyclic voltammograms (30 cycles in 30 min; 1

min/each cycle) of the G-ZnO-Au NC modified fluorine doped tin oxide (FTO) electrode under the same experimental conditions. The reductive current increasing at -1.05 V with each cycle reveals the formation of aniline. The electrocatalytic activity of G-ZnO-Au NC was found to be 1.5-fold higher in the presence of light when compared to that in the dark. These results show that the photocatalytic reaction did play a role in the enhanced reduction of NB to aniline.

4.3.3 Photoelectrocatalytic Reduction of Nitrobenzene

To gain more insight into the photocatalytic activity of G-ZnO-Au NCs toward NB, the current-time (I-t) curves were recorded at -0.45 V with and without illumination under UV light. The Fig. 4.8A displays representative *I-t* curves (12 cycles), with highly repeated results. The Fig. 4.8B shows the cyclic voltammograms of NB (5 mM) on an FTO (curve A) and G-ZnO-Au NC modified FTO electrode (curve B). The reductive current of NB on the G-ZnO-Au NC electrode at -1.2 V was 1.3 µA, while it was negligible when using a bare FTO, supporting great photocatalytic activity of the G-ZnO-Au NCs toward reduction of NB. As shown in curve B (Fig. 4.8B), NB started to reduce at −0.40 V (peak a) with an onset potential of -0.25 V. It is known that NB is primarily reduced to NSB, then PHA, and finally aniline. A cathodic peak was obtained at −1.05 V (peak b) which is attributed to the reduction of PHA to aniline. A small anodic hump at 0.2 V (peak c) was observed in the anodic scan which is paired with a less prominent cathodic peak at 0.25 V (peak d). The oxidation of PHA to NSB occurred at 0.2 V (peak c), while the reduction of NSB to PHA occurred at 0.25 V (peak d).[7] As can be seen in Fig. 4.8B, the peak related to the PHA reduction to aniline is located at − 1.05 V. It is seen that the current for peak (c) was higher than that of the peak (d), favoring a more direct reduction

71

pathway of NB to NSB to aniline in comparison to the reduction pathway having an intermediate step of the reduction from NSB to PHA to aniline.
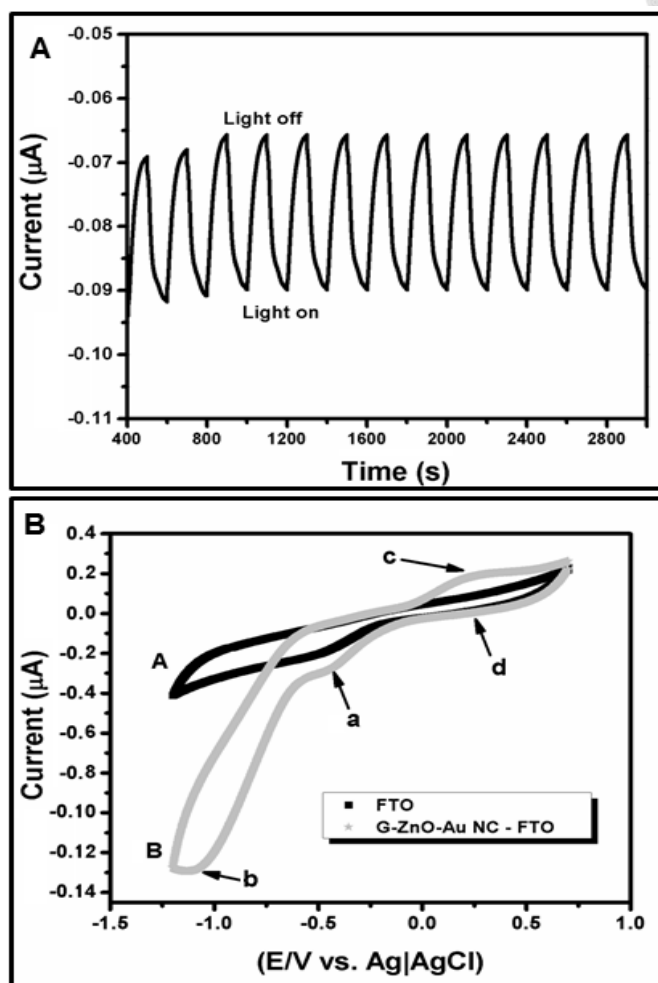
Fig. 4.8 (A) The photocurrent responses occurred at G-ZnO-Au NCs modified FTO for 12 repeated on-off cycles at an interval of every 200 s with an applied potential of -0.45 V. (B) Cyclic voltammograms obtained for the photoelectrocatalytic degradation of nitrobenzene on (A) bare FTO and (B) G-ZnO-Au NC- modified electrode. The corresponding peaks are (a) reduction of nitrobenzene, (b) reduction of PHA to aniline, (c) oxidation of PHA to NSB (d) reduction of NSB to PHA

72

To support this argument, we conducted SALDI-MS analyses of the products and intermediates of NB through photoelectrocatalytic and phototocataytic reactions using the G-ZnO-Au NCs.
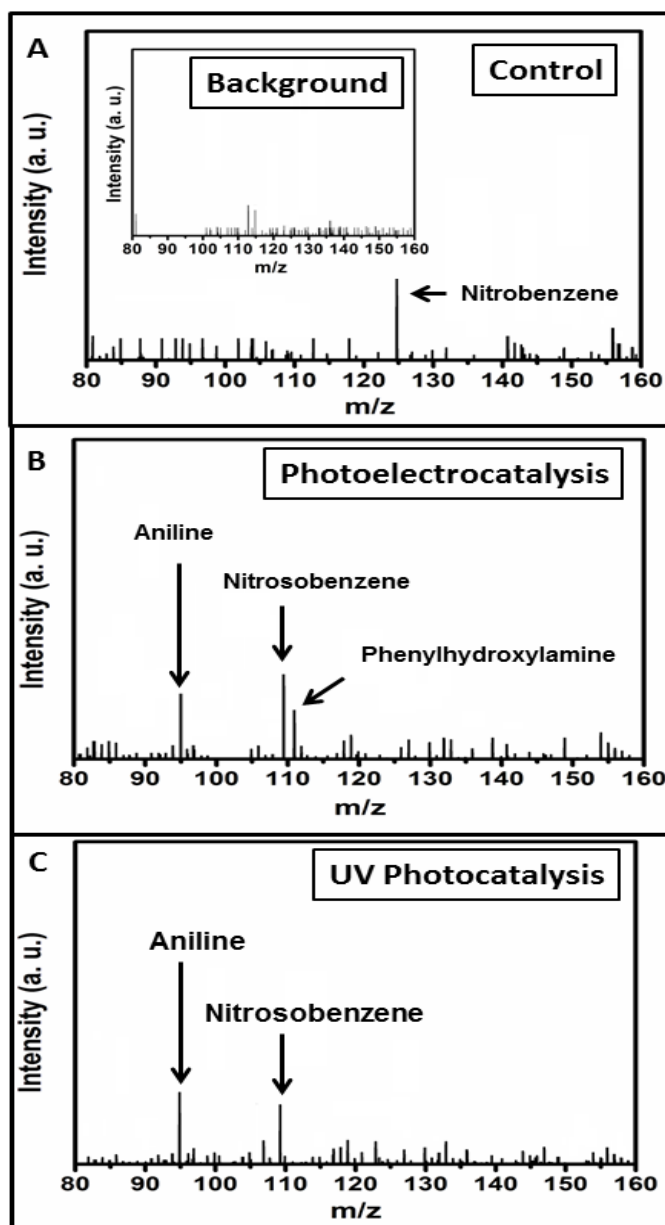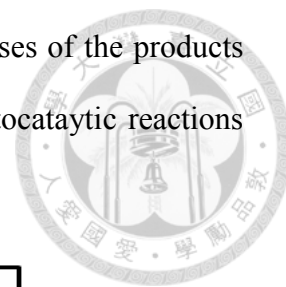
Fig. 4.9 SALDI-TOF MS spectra of the various products of nitrobenzene after 30 min of irradiation using G-ZnO-Au NCs through different reduction routes (A) control (B) photoelectrocatalysis and (C) UV light induced photocatalysis. Inset to (A) is background MS spectrum.   Nitrobenzene (5 mM) in methanol (50 mL) was used as a control.

Au nanoparticles as a matrix was used in this SALDI-MS analysis (Fig. 4.9).[42,43] The MS signals at *m/z* 124.730, 107.883, 110.902, and 94.886 are assigned for NB, NSB, PHA, and aniline, respectively. The Fig. 4.9A depicts the MS spectra of control showing only the NB peak in the absence of photocatalyst. In the case of the photoelectrocatalysis (Fig. 4.9B) there are two additional peaks for NSB and a less intense PHA peak along with one for aniline, which correlates to the favored product pathway obtained in the cyclic voltammogram, wherein NB was reduced to NSB and then to aniline. On the other hand, for the photocatalytic reduction of NB (Fig. 4.9C) the two peaks of NSB and aniline confirms the favored pathway of direct reduction of NB to aniline via NSB without the formation of PHA. Upon increasing the reaction time, the peaks for the NB, NSB, and PHA became smaller, while that for aniline increased. No peak for NB was observed after a reaction time of 140 min. Based on the MS results, we proposed that the reduction of NB using the G-ZnO-Au NCs under UV photocatalytic reduction was proposed to occur through route (1) as shown in Fig. 4.10, i.e.:
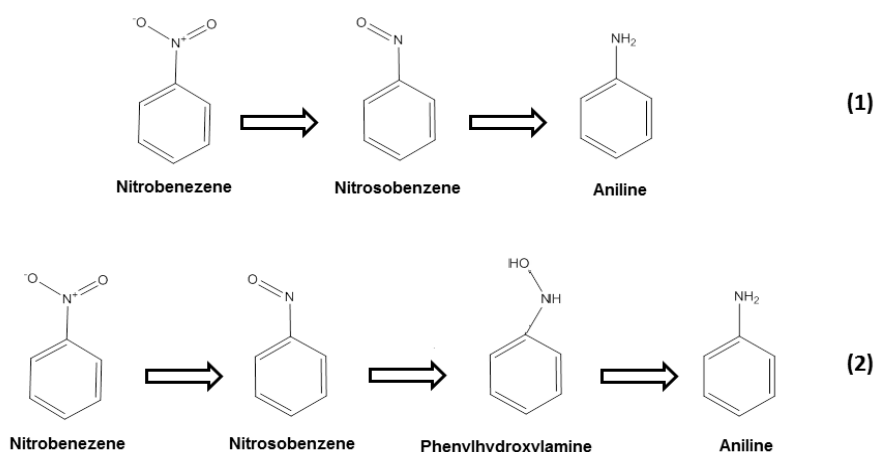
Fig. 4.10 Proposed pathways towards the formation of aniline from nitrobenzene using the G-ZnO-Au NCs under (1) UV photocatalysis and (2) photoelectrocatalysis.

NB to aniline via NSB without the formation of PHA could be ascribed to the fact that the degradation of NSB to PHA occurs at a rapid pace, while the conversion of PHA to aniline occurs at an even higher speed making it difficult to detect PHA.[6, 44] On the other hand, for UV photoelectrocatalytic reduction it follows route (2) where NB is reduced to aniline via NSB and PHA, due to PHA being quite stable at neutral pH which makes it difficult to be readily reduced into aniline at a rapid pace, allowing it to be more easily detected using SALDI- MS.[7]
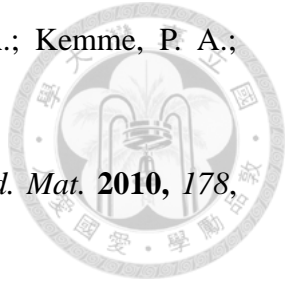
4.4 Conclusions

G-ZnO-Au NCs were used as photocatalysts for the reduction of NB to aniline, with conversion efficiency of 97.8% within 140 min. The contribution of graphene and Au NRs towards the photocatalytic activity of ZnO was studied; graphene acted as an inhibitor towards the h^+/e^- recombination, along with its excellent electron transport properties, and the Au NRs assisted in efficient charge separation. The pathways were studied by conducting SALDI-MS, which showed aniline as the major product in both photocatalytic and photoelectrocatalytic reductions of NB. This photocatalyst is green, efficient, and reusable for the reduction of NB, without producing toxic by-products. Our study opens up a new class of nanocomposites that can be used effectively to reduce NB and other potential nitroaromatic compounds used in the industry.

References

(1) N. A. Listed, Report on Carcinogens, National Toxicology Program, Research Triangle Park, NC, USA, 2011, 294-295.

(2) Colucci, J.; Montalvo, V.; Hernandez, R.; Poullet, C. *Electrochim. Acta.* **1999,** *44*, 2507-5021.

(3) Zhu, H.; Ke, X.; Yang, X.; Sarina, S.; Liu, H. *Angew. Chem. Int. Ed.* **2010,** *49*, 9657-9718.

(4) Chen, S.; Zhang, H.; Yu, X.; Liu, W. *Chin. J. Chem.* **2010,** *28*, 21-47.

(5) Shen, X.-Z.; Liu, Z.-C.; Xie, S.-M.; Guo, J. *J. Hazard. Mater.* **2009,** *162*, 193-1201.

(6) Flores, S. O.; Rios-Bernij, O.; Valenzuela, M. A.; Córdova, I.; Gómez, R.; Gutiérrez, R. *Top. Catal.* **2007,** *44*, 507-511.

(7) Li, Y.-P.; Cao, H.-B.; Liu, C.-M.; Zhang, Y. *J. Hazard. Mater.* **2007,** *148*, 158-163.

(8) Nishino, S. F.; Spain, J. C. *Appl. Environ. Microbiol.* **1993,** *59*, 2520-2525.

(9) Marvin-Sikkema, F. D.; Bont, J. A. M. *Appl. Microbiol. Biotechnol.* **1994,** *42*, 499-507.

(10) Mu, Y.; Yu, H.-Q.; Zheng, J.-C.; Zhang, S.-J.; Sheng, G.-P. *Chemosphere.* **2004,** *54*, 789-794.

(11) Bhatkhande, D. S.; Pangarkar, V. G.; Beenackers, A. A. C. M. *Water Res.* **2003,** *37*, 1223-1230.

(12) Liu, X.; Pan, L.; Lv, T.; Lu, T.; Zhu, G.; Sun, Z.; Sun, C. *Catal. Sci. Technol.* **2011,** *1*, 1189-2382.

(13) Datta, A.; Priyam, A.; Bhattacharyya, S. N.; Mukherjea, K. K.; Saha, A. *J. Colloid Interface Sci.* **2008,** *322*, 128-135.

(14) Makarova, O. V.; Rajh, T.; Thurnauer, M. C.; Martin, A.; Kemme, P. A.; Cropek, D. *Environ. Sci. Tech.* **2000,** *34*, 4797-4803.

(15) Huang, H.; Zhou, J.; Liu, H.; Zhou, Y.; Feng, Y. *J. Hazard. Mat.* **2010,** *178*, 994-998.

(16) Tada, H.; Ishida, T.; Takao, A.; Ito, S. *Langmuir* **2004,** *20*, 7898-7900.

(17) Huang, Y.; Ho, W.; Ai, Z.; Song, X.; Zhang, L.; Lee, S. *Appl. Catal., B: Environ.* **2009,** *89*, 398-405.

(18) Chatterjee, D.; Dasgupta, S. *J. Photochem. Photobiol. C.* **2005,** *6*, 186-205.

(19) Yao, W.; Iwai, H.; Ye, J. *Dalton Trans.* **2008**, 11, 1426-1430.

(20) Dikin, D. A.; Stankovich, S.; Zimney, E. J.; Piner, R. D.; Dommett, G. H. B.; Evmenenko, G.; Nguyen, S. B. T.; Ruoff, R. S. *Nature* **2007,** *448*, 457-460.

(21) Stoller, M. D.; Park, S.; Zhu, Y.; An, J.; Ruoff, R. S. *Nano Lett.* **2008,** *8*, 3498-3502.

(22) Xiang, Q.; Yu, J.; Jaroniec, M. *Chem. Soc. Rev.* **2012,** *41*, 782-796.

(23) Zhang, J.; Yu, J.; Jaroniec, M.; Gong, J. R. *Nano Lett.* **2012**, *12*, 4584-4589.

(24) Li, Q.; Guo, B.; Yu, J.; Ran, J.; Zhang, B.; Yan, H.; Gong, J. R. *J. Am. Chem. Soc.* **2011**, *133*, 10878-10884.

(25) Xiang, Q.; Yu, J. *J. Phys. Chem. Lett.* **2013,** *4,* 753–759.

(26) Toh, H. S.; Ambrosi, A.; Pumera, M. *Catal. Sci. Technol.* **2012,** *3,* 123-127.

(27) Han, L.; Wang, P.; Dong, S. *Nanoscale* **2012**, *4,* 5814-5825.

(28) Maeda, K.; Teramura, K.; Lu, D.; Takata, T.; Saito, N.; Inoue, Y.; Domen, K. *Nature* **2006,** *440*, 295-295.

(29) Yu, J.; Yu, X. *Environ. Sci. Technol.* **2008,** *42*, 4902-4907.

(30) Xu, T.; Zhang, L.; Cheng, H.; Zhu, Y. *Appl. Catal. B. Environ.* **2011,** *101*, 382-387.

(31) Huang, C. C.; Yang, Z.; Chang, H. T. *Langmuir* **2004,** *20*, 6089-6092.

(32) Wu, J.; Shen, X.; Jiang, L.; Wang, K.; Chen, K. *Appl. Surf. Sci.* **2010,** *256*, 2826-2830.

(33) Murphy, C. J.; Thompson, L. B.; Chernak, D. J.; Yang, J. A.; Sivapalan, S. T.; Boulos, S. P.; Huang, J.; Alkilany, A. M.; Sisco, P. N. *Curr. Opin. Colloid Interface Sci*. **2011**, *16*, 128-134

(34) Hu, Y.; Jin, J.; Wu, P.; Zhang, H.; Cai, C. *Electrochim. acta.* **2010,** *56*, 491-500.

(35) Song, W. T.; Xie, J.; Liu, S. Y.; Zheng, Y. X.; Cao, G. S.; Zhu, T. J.; Zhao, X. B. *Int. J. Electrochem. Sci.* **2012,** *7*, 2164-2174.

(36) Lv, T.; Pan, L.; Liu, X.; Sun, Z. *Catal. Sci. & Tech.* **2012**. *509*, 10086-10091.

(37) Zhu, Z.; Chen, T. L.; Gu, Y.; Warren, J.; Osgood Jr, R. M. *Chem. Mater.* **2005,** *17*, 4227-4234.

(38) Dhara, S.; Giri, P. K. *J. App. Phys.* **2011**, *110*, 124317-1-124317-9.

(39) Dhara, S.; Giri, P. *Nanoscale Res. Lett.* **2011,** *6*, 1-8.

(40) Gai, P. L.; Harmer, M. A. *Nano Lett.* **2002,** *2*, 771-774.

(41) Tan, T.; Beydoun, D.; Amal, R. *J. Photochem. Photobiol., A. Chem.* **2003,** *159, 273-280.*

(42) Zhang, H.; Lv, X.; Li, Y.; Wang, Y.; Li, J. *ACS Nano* **2009,** *4*, 380-386.

(43) Brezová, V.; Tarábek, P.; Dvoranová, D.; Staško, A.; Biskupič, S. *J. Photochem. Photobio.A*. **2003**, *155*, 179-198.

(44) Yang, N.; Zhai, J.; Wang, D.; Chen, Y.; Jiang, L. *ACS Nano* **2010,** *4*, 887-894.

(45) Tang, Y.-B.; Lee, C.-S.; Xu, J.; Liu, Z.-T.; Chen, Z.-H.; He, Z.; Cao, Y.-L.; Yuan, G.; Song, H.; Chen, L.; Luo, L.; Cheng, H.-M.; Zhang, W.-J.; Bello, I.; Lee, S.-T. *ACS Nano.* **2010,** *4*, 3482-3488.

(46) Primo, A.; Corma, A.; Garcia, H. *Phys. Chem. Chem. Phys.* **2011,** *13*, 886-910.

(47) Huber, E. *Appl. Phys. Lett.* **1966,** *8*, 169-171.

(48) Hsieh, Y-P.; Liang, C-T.; Chen, Y-F.; Lai, C-W.; Chou, P-T. *Nanotechnol.* **2007,** *18*, 415707-1-415707-4.

(49) Brillas, E.; Banos, M. A.; Camps, S.; Arias, C.; Cabot, P.-L.; Garrido, J. A.; Rodriguez, R. M. *New J. Chem.* **2004,** *28*, 314-322.

(50) Auer, E.; Freund, A.; Pietsch, J.; Tacke, T. *Appl. Catal., A. General.* **1998,** *173*, 259-271.

(51) Chen, W.-T.; Chiang, C.-K.; Lin, Y.-W.; Chang, H.-T. *J. Am. Soc. Mass Spectrom.* **2010,** *21*, 864-867.

(52) Huang, Y. F.; Chang, H. T. *Anal. Chem.* **2006,** *78*, 1485-1493.

(53) Piccinini, P.; Minero, C.; Vincenti, M.; Pelizzetti, E. *J. Chem. Soc., Faraday Trans.* **1997,** *93*, 1993-2000.

Chapter 5

Summary and Perspective

5.1 Summary

Chapter one introduces the role of nanotechnology from its evolution to the present day and the multifaceted areas of research that has manifested itself. A brief explanation about the various aspects of research carried out in this thesis was outlined from bio sensors used for colorimetric sensing to semiconductor photocatalysts used for environmental remediation. The second chapter focuses on the synthesis of FeTe NRs prepared from Tellurium nanowires through a galvanic reaction with the cynosure on colorimetric sensing of glucose in blood at high sensitivity (55 nM). The enzyme mimicking FeTe NRs having high catalytic activity for the peroxidase substrate ABTS were synthesized from Te NWs through a galvanic reaction. FeTe NRs were also found to have a higher enzyme activity in comparison to those of HRP and Fe_3O_4 NPs due to amount of Fe(II) ions on their surfaces, enabling the use of FeTe NRs as enzyme mimics for the detection of various analytes of interest when suitable enzymes are used to generate H_2O_2. The third chapter carries forward this concept of colorimetric bio-sensing using FeTe NRs through detecting mercury in blood as the FeTe NRs were displaced by Hg^{2+} ions to form HgTe mainly due to a cation exchange mechanism. The sensing approach was validated by the determination of the concentration of total Hg in a blood sample (SRM 955c). The final chapter focusses on the synthesis of semiconductor photocatalyst (G-ZnO-Au NCs) for the reduction of nitrobenzene to aniline, with conversion efficiency close to 100% within 140 min. This green, efficient and reusable photocatalyst reduced nitrobenzene, without producing any toxic by-products, showing the effectiveness of using this new class of nanocomposite materials capable of utilizing solar energy effectively to reduce nitrobenzene and other potential aromatic compounds used in the industry.

5.2 Perspective

Biosensing has taken significant strides over the last few decades due to the advancement in nanomaterials that have been designed and fabricated for specific applications. Iron based nanomaterials such as FeTe NRs provide a cheaper alternative to gold and other similar noble nanomaterials and a useful platform for a wide range of biosensing applications. These newly developed FeTe NRs have shown great advantages over conventional assays, particularly in sensitivity, selectivity, and practicality largely due to its low cost, simplicity, and practicality in addition to robust physical as well as chemical properties of these materials making them promising candidates for colorimetric biosensing.

The next challenge for FeTe NRs would be to develop simple, rapid, and inexpensive detection assays for monitoring of food and water contamination by bacteria and other pathogens, diagnostic applications, and environmental analysis. There is a need to build glucose sensors that utilize "test strips", particularly so for the developing world, which does not have ready access to laboratory facilities. The fact that FeTe NRs have high thermal stability allows them to be used in geographically hot areas, where biomolecules might undergo thermal denaturation at elevated temperatures (e.g., above 45 °C), leading to loss of sensitivity in traditional bioassays. FeTe NRs can be implemented as dipsticks or in a chromatographic format, the color change observed through the naked eye absolves the need for sophisticated instrumentation.

Another immediate challenge to be met is to functionalize the FeTe NRs with unique optical signatures with different receptors. We foresee that this will enable them to have a unique optical response to biomolecular binding thus allowing detection of various analytes. Finally one can incorporate the FeTe NRs into a nano/micro fluidics channel. The integration of with a lab-on–a-chip bioanalytical devices will enable the

ultrasensitive detection of a large number of analytes in a single device.
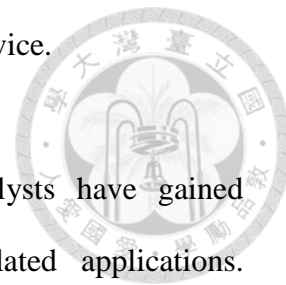
On the other hand, Graphene-based semiconductor photocatalysts have gained traction due their potential in environmental and energy-related applications. Although considerable progress has been achieved, the studies in this field are at a nascent stage and further developments are required. To begin with, the preparation of graphene is still maturing and there are a variety of issues that requires attention. There is a need for preparing pure and bulk graphene in cheap and environmentally friendly manner with tunable sizes of layers, compositions and defects. Next, we should be able to tune the performance of graphene-based semiconductor composites by varying the loading of each of the composites. Therefore, there is need for precisely designed composites by achieving uniform morphology to enhance the photocatalytic properties. Finally, an aspect of graphene based semiconductor photocatalysts that has not received great attention is the mechanism and remains to be discussed further. For instance, the exact role of graphene in enhancing the mechanism still remains debatable. Furthermore there is a need to determine the exact mechanistic pathway behind the photocatalytic activity for different semiconductor photocatalysts such as ZnO or TiO_2 or noble metal photocatalysts such as gold.

To summarize, we must meet the challenge of fabricating pure carbon and carbon-based composites for the purpose of photocatalytic reduction or oxidation. The perspective is to focus on the principle and the development of photocatalysis in carbon-based nanomaterials synthesis. This needs to be application-driven, but the challenge to further develop the field rests between a simultaneous study of the fundamental processes and a better control of the synthetic routes.
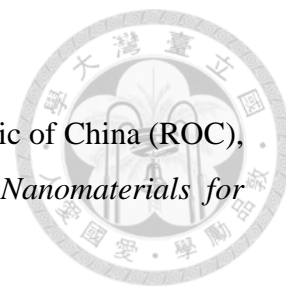
Publications

(1) Roy, P.; Tsai, T. C.; Liang, C.-T.; Wu, R. J.; Chavalia, M., Application of Impedance Measurement Technology in Distinguishing Different Tea Samples with Ppy/SWCNT Composite Sensing Material. *J. Chin. Chem. Soc.* **2011,** *58*, 714-722.

(2) Yang, Z.; Chen, C.-Y.; **Roy, P**.; Chang, H.-T., Quantum dot-sensitized solar cells incorporating nanomaterials. *Chem. Commun.* **2011,** *47*, 9561-9571.

(3) Roy, P.; Lin, Z.-H.; Liang, C.-T.; Chang, H.-T., Synthesis of enzyme mimics of iron telluride nanorods for the detection of glucose. *Chem. Commun.* **2012,** *48*, 4079-4081.

(4) Lee, Y.-F.; Deng, T.-W.; Chiu, W.-J.; Wei, T.-Y.; **Roy, P**.; Huang, C.-C., Visual Detection of Copper (II) Ions in Blood Samples by Controlling the Leaching of Protein-Capped Gold Nanoparticles. *Analyst* **2012**, *137*, 1800-1806.

(5) Roy, P.; Lin, Z.-H.; Liang, C.-T.; Chang, H.-T., Iron telluride nanorods-based system for the detection of total mercury in blood. *J. Hazard. Mater.* **2012**, 24*3*, 286-291.

(6) Lin, Z. H.; Shih, Z. Y.; **Roy, P**.; Chang, H. T., Preparation of Photocatalytic Au–Ag$_2$Te Nanomaterials. *Chem,-A Eur. J.* **2012**, *18*, 12330-12336.

(7) Lin, Z. H.; **Roy, P**.; Shih, Z. Y.; Ou, C. M.; Chang, H. T., Synthesis of Anatase Se/Te-TiO2 Nanorods with Dominant {100} Facets: Photocatalytic and Antibacterial Activity Induced by Visible Light. *ChemPlusChem* **2013**, *78,* 302-309.

(8) Roy, P.; Periasamy, A. P.; Liang, C.-T.; Chang, H.-T., Synthesis of Graphene-ZnO-Au Nanocomposites for Efficient Photocatalytic Reduction of Nitrobenzene. *ACS Environ. Sci and Tech.* **2013**, 47, 6688-6695

Books

(1) Chen, P.-C.; <u>**Roy, P**</u>.; Chen, L.-Y.; Chen, Y.-N.; Chang, H.-T., "Gold Nanomaterials Based Absorption and Fluorescence Detection of Mercury, Lead, and Copper", *Interactions of Nanomaterials with Emerging Environmental Contaminants,* **2013.**

(2) <u>**Roy, P**</u>.; Periasamy, A. P.; Liang, C.-T.; Chang, H.-T., "Photoluminescent Graphene Quantum Dots: synthetic routes, unique physicochemical properties and bio-application", *Handbook of Graphene Science. Volume 4,* Chapter 15, **2013.**

Conferences

(1) 2010 Annual Meeting of the Physical Society of the Republic of China (ROC), February 2010, Tainan, Taiwan. *"Preparation of Smart Nanomaterials for Energy Applications"*.

(2) 2010 Annual Meeting of Chinese Chemical Society, December 2010, Taipei, Taiwan. *"Synthesis of Smart Nanomaterials for Sensing Applications"*.

(3) 2011 Annual Meeting of Chinese Chemical Society, December 2011, Hsinchu, Taiwan *"Iron Telluride based Nanomaterials for Sensing Glucose and Mercury in Blood"*.

(4) National Institute of Material Science Conference, June 2012, Tsukuba, Japan. *"Enzyme Mimicking Iron Telluride based Nanorods for the Detection of Glucose"*.

(5) Indo-Taiwan Research Talk on Smart Nanomaterials, August 2012, Kanyakumari, India. *"Iron Telluride and Graphene Based Nanomaterials for Sensing and Photocatalytic Applications"*.

(6) 2012 Annual Meeting of Chinese Chemical Society, December 2012, Tainan, Taiwan. *"Graphene Based Semiconductor Nanocomposites for Photocatalytic Applications"*.

(7) Annual NTU Chemistry Graduate Research Sympsoium, December 2012, Taipei, Taiwan. *"Iron Telluride and Graphene Based Nanomaterials for Sensing and Photocatalytic Applications"*.